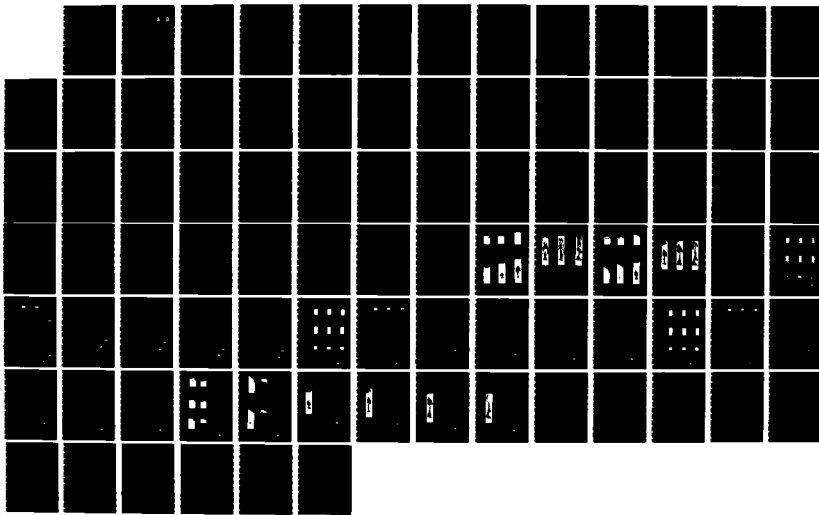


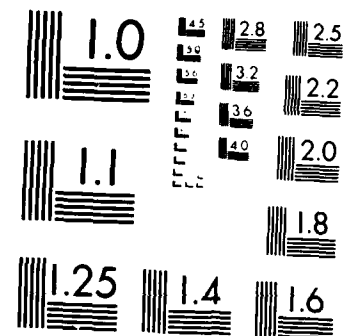
AD-A175 848 COMPUTER MODELLING OF TWO-PHASE FLOW(U) IMPERIAL COLL  
OF SCIENCE AND TECHNOLOGY LONDON (ENGLAND) S M FARWAGI 1/1  
OCT 86 R/D-4107-AN DRJA45-83-C-0027

UNCLASSIFIED

F/G 20/4

NL





PHOTOCOPY RESOLUTION TEST CHART  
NATIONAL BUREAU OF STANDARDS 1963-A

AD-A175 048

(4)

FINAL REPORT

on

DTIC  
ELECTED  
DEC 12 1986  
S D

COMPUTER MODELLING OF TWO-PHASE FLOW

Author	S M Farwagi
Supervisor	Professor D B Spalding Head, CFDU Imperial College Exhibition Road London SW7
Date	October 1986
Research Sponsor	U.S. Army (European Research Office)
Sponsors Ref.	DRXN-UK-RA-R&D4107AN DAJA 45-83-C0027
Imperial College Ref.	4C.13

DTIC FILE COPY

APPROVED FOR PUBLIC RELEASE; DISTRIBUTION UNLIMITED

## UNCLASSIFIED

R&amp;D 4107-AN

SECURITY CLASSIFICATION OF THIS PAGE (When Data Entered)

REPORT DOCUMENTATION PAGE		READ INSTRUCTIONS BEFORE COMPLETING FORM
1. REPORT NUMBER	2. GOVT ACCESSION NO.	3. RECIPIENT'S CATALOG NUMBER
<b>AD-AM5048</b>		
4. TITLE (and Subtitle)  Computer Modelling of Two-Phase Flow	5. TYPE OF REPORT & PERIOD COVERED  Final Technical Report Dec 82 - Oct 86	
7. AUTHOR(s)  S.M. Farwagi	6. PERFORMING ORG. REPORT NUMBER  DAJA45-83-C-0027	
9. PERFORMING ORGANIZATION NAME AND ADDRESS  Imperial College Exhibition Road, London SW7	10. PROGRAM ELEMENT, PROJECT, TASK AREA & WORK UNIT NUMBERS  61102A 11161102BH57-06	
11. CONTROLLING OFFICE NAME AND ADDRESS  USARDSG-UK Box 65, FPO NY 09510-1500	12. REPORT DATE  October 1986	
14. MONITORING AGENCY NAME & ADDRESS (if different from Controlling Office)	13. NUMBER OF PAGES  86	
	15. SECURITY CLASS. (of this report)  Unclassified	
	15a. DECLASSIFICATION/DOWNGRADING SCHEDULE	
16. DISTRIBUTION STATEMENT (of this Report)  Approved for Public Release; distribution unlimited		
17. DISTRIBUTION STATEMENT (of the abstract entered in Block 20, if different from Report)		
18. SUPPLEMENTARY NOTES		
19. KEY WORDS (Continue on reverse side if necessary and identify by block number)  Computer simulations. Two-phase flow. Rayleigh-Taylor Instability. Gun-barrel phenomena		
20. ABSTRACT (Continue on reverse side if necessary and identify by block number)  In the accelerating flow of a lighter continuous phase through a heavier one, small non-uniformities grow into large ones due to the Rayleigh-Taylor Instability. An experiment exemplifying the large 'bubble' formation due to Rayleigh-Taylor Instability has been performed and simulated using the PHOENICS 84 computer code. The same numerical procedure was applied to the two-phase flow in a gun barrel. It showed that the acceleration provided by the movement of the projectile can cause initial non-uniformities to grow with time.		

ABSTRACT

In the accelerating flow of a lighter continuous phase through a heavier one, small non-uniformities grow into large ones due to the Rayleigh-Taylor Instability. An experiment exemplifying the large 'bubble' formation due to Rayleigh-Taylor Instability has been performed and simulated using the PHOENICS 84 computer code. The same numerical procedure was applied to the two-phase flow in a gun barrel. It showed that the acceleration provided by the movement of the projectile can cause initial non-uniformities to grow with time.



Accession For	
NTIS CRA&I	<input checked="" type="checkbox"/>
DTIC TAB	<input type="checkbox"/>
Unannounced	<input type="checkbox"/>
Justification	
By	
Distribution	
Availability Codes	
Avail. Add. or	
Dist. Special	
A-1	

## CONTENTS

1. Introduction
2. Objectives of the Work
3. Outline of the Report
4. Experimental Work
  - 4.1 Experiment with a Flat Interface
    - 4.1.1 Apparatus
    - 4.1.2 Procedure
    - 4.1.3 Observations
  - 4.2 Experiment with a Tilted Interface
    - 4.2.1 Apparatus
    - 4.2.2 Procedure
    - 4.2.3 Observations
  - 4.3 Discussion
5. Numerical Prediction of the Experiment
  - 5.1 Governing Equations
  - 5.2 The numerical solution procedure
  - 5.3 Parametric Studies
    - 5.3.1 The Effect of the Interphase Friction Coefficient
    - 5.3.2 The Effect of Viscosity
    - 5.3.3 The Effect of the Wall
    - 5.3.4 Conclusions
  - 5.4 The Prediction of the Experiment with a Tilted Interface
  - 5.5 Discussion
  - 5.6 Conclusions
6. Numerical Simulation of the gun-barrel situation
  - 6.1 Introduction
  - 6.2 The Physical Problem
  - 6.3 The Dependent and Independent Variables
  - 6.4 The Partial Differential Equations

- 6.4.1 The Mass Conservation Equation
- 6.4.2 The Conservation of Momentum Equations
- 6.4.3 The Conservation of Energy Equations

## 6.5 Auxilliary Relations

- 6.5.1 The Equation of State
- 6.5.2 The Intergranular Stress
- 6.5.3 The Interphase Friction Coefficient
- 6.5.4 The Particle Burning Rate
- 6.5.5 Ignition Criterion
- 6.5.6 The Interphase Heat Transfer Coefficients
- 6.5.7 The Movement of the Projectile

## 6.6 The Problem considered.

## 6.7 Computational Details

## 6.8 Results

- 6.8.1 Simulation of the gun barrel situation
- 6.8.2 The effect of an initial non-uniformity
- 6.8.3 Discussion

## 6.9 Conclusions

## 7. Future Work

## 8. Nomenclature

## 9. References

## 1. INTRODUCTION

In the accelerating flow of a lighter continuous phase through a heavier one, non-uniformities grow in size due to the Rayleigh-Taylor Instability (RTI) forming large low-particle-density 'bubbles' moving through high-particle-density fluids.

The RTI (Ref. 1) has for a long time been recognised when the two phases are liquids with differing densities. Several authors have demonstrated the growth of small perturbances into large ones in experiments where for example: a heavy fluid falls through a lighter one under gravity (Refs. 2, 3 and 4); or when a lighter fluid rests on top of a heavier one and the binary fluid system is accelerated downwards at a rate greater than that of gravity (Ref. 5 and 6).

In a similar manner, a gas accelerating through a bed of particles is expected to act on non-uniformities in the particle packing distribution causing them to grow in size. Such a situation is encountered in guns where the acceleration is provided by the projectile movement which drags the gas (and combustion products) with it. The RTI then acts on non-uniformities present in regions of the gun barrel where unburned or partly burnt particles exist causing them to grow.

The presence of bubbles in guns would cause irregularities in the rate of combustion of the particles. The transfer of heat in the flow would also be affected since the mechanism of heat transfer within the bubble is predominantly convective rather than conductive. Also, the bubbles would appreciably affect the radial velocities of the unburnt or partly burnt particles thus

influencing the heat transfer to and erosion of the barrel walls.

## 2. OBJECTIVES

The objectives of the present work are:-

- (a) Devise a simple experiment which will exemplify the formation of low particle density bubbles which move through high-particle-density fluids;
- (b) Devise a computer model which simulates the observed phenomena with sufficient accuracy;
- (c) Use this model with appropriate changes in the initial and boundary conditions and in the material properties to explore the likelihood of Rayleigh-Taylor instability in guns.

## 3. OUTLINE OF THE REPORT

Section 4 of this report describes the experimental work carried out while section 5 gives the results of the simulation of the experiment using the PHOENICS 84 computer code. In section 6, a computer model is presented for simulating combustion in a gun. The results are discussed and recommendations for future work are given in section 7.

## 4. EXPERIMENTAL WORK

Experiments are considered essential since they: (i) ensure that all the processes relevant to the problem in question are accounted for in the numerical model; and (ii) they yield basic experimental data for comparison with the numerical predictions

thus providing an important feedback to the model and a measure of its accuracy.

In the present work, simple experiments were performed to investigate the Rayleigh-Taylor phenomenon. In these experiments, water was used to accelerate through a bed of sand in a 2D glass channel. Using water is not unrealistic since in guns, the density of the gas producing the acceleration is comparable to the density of the propellant particles. In these experiments, the water enters the bed of sand through a porous side wall. This to some extent, simulates in the laboratory, the situation in guns where the gas producing the acceleration comes from a distributed source which is the burning of the propellant particles.

Two different experiments have been performed. In the first, the interface of the bed of sand is flat while in the second it is tilted. In the first experiment, the R-T acts upon inherent non-uniformities in the particle packing distribution while in the second an additional initial disturbance is imposed through tilting the interface. These two experiments are described in the following sections.

#### 4.1 Experiment with a Flat Interface

##### 4.1.1 Apparatus

A schematic diagram of the rig is shown in Figure 1. A piece of fine wire gauze, fitted in a metal frame, forms part of the back wall of a channel made up of two glass plates 15cm wide and 100cm long. The glass plates are separated by a gap of

1.5cm. A head tank placed approximately 3m above the sand provides the pressure head required to push the water through the sand. The sand particles are about 100 $\mu$ m and have a density of 2,500kg/m<sup>3</sup>. Glass beads are introduced as shown in Figure 1 to break down the turbulence eddies at entry and to produce a more uniform flow across the channel.

A video system capable of 25 frames/second was used to record the observations. This permitted an immediate real time or frame-by-frame replay of each run. The photographs presented in this report were taken with a 35mm camera fitted with a motor drive capable of 5 frames/second.

The water in the tank was dyed blue using nigrosene. The top surface of the water was therefore always discernible enabling its velocity to be measured at all times.

#### 4.1.2 Procedure

Sand is poured through the open top of the channel to the desired height. The valve (A) (see Figure 1) is then slowly opened to allow water into the channel, setting the particles into motion and expelling the air bubbles trapped within the sand bed. When the water reaches the top of the channel, valve (A) is closed and the sand allowed to settle. Then valve (B) is opened to drain the water from the channel but not enough for the water level to fall below the height of the sand bed. This operation is repeated several times until all the air traps have been expelled from the system.

The settling of the sand after the water inlet valve had been closed, never left a flat sand interface. The surface of

the sand bed sometimes formed a sinusoidal wave whose wavelength was similar to the width of the channel but it was often a series of random small waves forming an irregular wavy sand bed surface. To produce a flat interface whenever recording the observations, the side of the channel was gently tapped and although these irregular waves at the top of the sand bed disappeared this does not mean that the sand 'packing' in the bulk of the sand bed was uniform. It is these non-uniformities that get the Rayleigh-Taylor Instability started.

#### 4.1.3 Observations

The observations made are shown in Figure 2. At  $t = 0s$ , the initial water and sand levels can be seen prior to valve opening. This photograph also shows in the background, some of the equipment that was used in the experiment. This should be ignored. Upon opening the valve, the bed expands particulate without the appearance of any bubbles in it. The top surface of the bed curves upwards to form a convex surface at  $t = 0.2s$  but then oscillates and at  $t = 0.6s$  forms a concave surface. At  $t = 0.8s$ , a bubble is observed in the main body of the bed. This bubble grows with time. With the velocity in the bubble being higher than the surrounding mixture, a shear instability of the Kelvin-Helmholtz type develops. This occurs at  $t = 1.0s$  with the typical mushroom shapes appearing. Two velocity recirculation regions or vortices form near each of the walls. These regions grow with time until the two emanating from the opposite walls meet in the middle of the channel at  $t = 1.2s$ . Meanwhile the

leading edge of the bubble moves further up the channel. At  $t = 1.4s$ , a somewhat chaotic behaviour is observed where the sand which has been brought into the centre of the channel, is being penetrated by the water. But at  $t = 1.6s$ , a more orderly state is restored where three wavelengths of the Kelvin-Helmholtz instability can be seen along the right hand wall.

#### 4.2 Experiment with a Tilted Interface

The Rayleigh-Taylor instability acts upon non-uniformities in the flow and causes them to grow. In the experiment described in section 4.1, such non-uniformities are present but they are too small to quantify. These non-uniformities arise due to perhaps slight unintentional deviations of the channel from the vertical or from the uneven rate of sedimentation of the sand across the channel width (see Section 4.1.2).

This however, presents a problem when the R-T process is to be modelled. Unless non-uniformities are specified as initial conditions, the calculations will not show any growth of the R-T instability. An experiment was therefore carried out in which an initial disturbance was imposed. This disturbance was introduced by having an initially tilted sand interface. This could be easily specified as an initial condition in the numerical calculations.

##### 4.2.1 Apparatus

The same apparatus used for the flat interface experiments was used here. However, the procedure was changed to produce an initially tilted sand interface. This is described in the next

sub-section.

#### 4.2.2 Procedure

Sand is poured through the open top of the channel. The channel is then tilted by approximately  $10^{\circ}$  to the vertical. Valve (A) (see Figure 1) is then slowly opened, letting water into the test section and expelling the air bubbles which are trapped in the sand bed. When the water reaches the top of the test section, the valve (A) is closed and the sand allowed to settle. The valve (B) is then opened to drain the water from the channel but not enough for the water level to fall below the level of the bed of sand. This procedure is repeated several times until all the trapped air is expelled from the system. The channel is then set vertical but the interface of the sand bed remains at approximately  $10^{\circ}$  tilt.

As in the flat interface experiment, the settling of the sand was not uniform. Ripples always appeared at the surface of the sand bed and these were eliminated from the surface of the bed by gently tapping the side of the channel.

#### 4.2.3 Observations

The observations made are shown in Figure 3. At  $t = 0s$ , the initial tilted sand surface can be seen. The equipment showing in the background should be ignored. Upon opening the valve, the shallower part of the sand bed accelerates at a faster rate ( $t = 0.2s$ ) and a 'bulge' appears in the left hand side of the channel ( $t = 0.4$  and  $0.6s$ ). At  $t = 1.0s$ , the first traces of a bubble

appear which grows with time. Also, recirculation regions form near the wall due to K-H instability. The K-H instabilities grow as the leading edge of the bubble moves further up the channel ( $t = 1.2s$ ). At  $t = 1.4s$ , the recirculation zones near the wall are seen to be stretched and at  $t = 1.6s$ , a 'roll-over' wave on the right-hand side wall of channel is observed.

#### 4.3 Discussion

Two experiments have been described above. Despite the difference in the initial conditions, the size of the produced bubble and its velocity are in the two experiments similar. This can be explained by referring to the basic theory of the Rayleigh-Taylor instability. (Ref. 1). Under R-T instability, the growth rate of a wave is dependent on the density ratio of the two phases, the acceleration and the wavenumber of the disturbance i.e.

$$n^2 = At g k$$

where

$n$  is the growth rate

$At$  is the Atwood Number given by

$$At = \frac{\rho_2 - \rho_1}{\rho_2 + \rho_1}$$

and  $k$  is the wavenumber given by

$$k = \frac{2\pi}{\lambda}$$

where  $\lambda$  is the wavelength of the disturbance.

However, in any system certain wavelengths are more unstable than others and therefore grow faster. These critical, fast growing wavelengths are determined by the characteristics of the

system such as viscosity or surface tension. In the present experiments, it is the viscosity that plays this important role and the most unstable wavelengths grow faster to engulf the smaller ones. In the end, a dominant size of bubble emerges which is restricted by the width of the channel.

The velocity of a bubble moving up a channel is determined by the bubble size and the fluid acceleration (Refs. 5 and 7). Since in the two experiments, the bubble size is similar, its velocity is also expected to be similar.

Another feature which is common to the two experiments is the appearance of the velocity recirculation regions near the walls due to the K-H instability. This arises due to the velocity difference between the liquid in the bubble and the sand layers on its borders. In the two experiments, the velocity of the bubble is similar.

The experiment with a tilted interface is suitable for testing the predictions of PHOENICS with regards to the growth of the R-T instability. These predictions are given in the next section.

##### 5. The Numerical Prediction of the Experiment

Despite the apparent simplicity of the experiment, the numerical task is quite complex. Not only is the situation two-phase and two-dimensional, it also involves specifying interphase transport relationships. Due to the physical uncertainty regarding these processes and to the consequent lack of generalised models, a numerical study was carried out to determine the influence and relative importance of viscosity, the

interphase friction coefficient and the effect of the wall. This investigation is reported in section 5.3. In the following section, the two-phase two-dimensional balance equations solved using the PHOENICS computer code, are given.

### 5.1 Governing Equations

In the absence of the transfer of mass, the phase mass conservation or continuity equation is given by:-

$$\frac{\partial}{\partial t} \rho_i R_i + \text{div}(\rho_i R_i \langle v_i \rangle) = 0 \quad (5.1)$$

where

$\rho$  is the density

$R$  is the volume fraction

$\langle v \rangle$  is the velocity vector

and the subscript  $i$  refer to the phase in question i.e. liquid or solid.

The momentum equation is given by:-

$$\begin{aligned} \frac{\partial}{\partial t} (\rho_i R_i \phi) + \text{div} \{ R_i (\rho_i \langle v_i \rangle \phi - \mu \text{grad } \phi) \} \\ = R_i (F_g - \text{grad } p) + F_i + F_w \end{aligned} \quad (5.2)$$

where

$\phi$  stands for  $v_i$  and  $w_i$  the velocities in the radial and axial directions, respectively

$\mu$  is the dynamic viscosity

$F_g$  is the gravity source

$p$  is the pressure

$F_w$  is the wall friction

and

$F_i$  is the interphase friction

The expressions used for  $F_i$ ,  $\mu$  and  $F_w$  are given below in sections 5.3.1, 5.3.2 and 5.3.3 respectively. First, however, a brief description of the numerical solution procedure embodied in the PHOENICS 84 code is given.

## 5.2 THE NUMERICAL SOLUTION PROCEDURE

The above equations were solved using the PHOENICS 84 computer code (Refs. 8, 9 and 10).

A conventional staggered grid is used where the velocities are stored at the centre of the cell faces to which they are normal while all other variables are stored at the centres of the cells themselves.

The velocity locations have their own surrounding cells, which act as control volumes over which the differential momentum equations are integrated, to yield the corresponding finite domain equations for velocity. Equations for the other dependent variables employ control volumes around the grid points.

The result of the integration is a set of finite-domain equations which include contributions from the transient, convection, diffusion and source terms. Upwind differencing is used in evaluating the convection terms. A fully implicit formulation is used.

The finite-domain equations are solved using the SIMPLEST and IPSA algorithms (Ref. 10). The integration proceeds along the Z direction (see Figure 5) from the bottom to the top, and is repeated until convergence is achieved. Further details may be

found in the above references.

### 5.3 Parametric Studies

Preliminary calculations have established that unless an initial disturbance is specified, a bubble would not form. In other words, if the volume fraction distribution in the calculations is initially specified as being uniform everywhere, then a bubble would not form. Therefore in all the calculations given in this section an initial sinusoidal disturbance was imposed. The wavelength of this disturbance was equal to the channel width and its amplitude was a mere 0.001m. An exaggerated view of this disturbance is shown in Figure 4.

Due to the symmetry in the calculations, only half the channel was considered thus enabling higher accuracy for the same number of calculation cells. The half channel considered was divided into 15 and 48 cells in the lateral and axial directions respectively. A part fixed moving grid was used (Ref. 11) as illustrated in Figure 5.

The parameters thought to be of importance that were investigated were the interphase friction factor, the viscosity and the wall friction.

#### 5.3.1 The Effect of the Interface Friction Coefficient

The relative velocity between the two phases is determined by the interphase friction force given by:-

$$F_i = FIP (V_1 - V_2) \quad (5.3)$$

where FIP is the interphase transport coefficient per unit volume given by:-

$$FIP = CFIPS \times \rho_1 \times R_1 \times R_2$$

where the subscripts 1 and 2 refer to the light and heavy phases respectively and CFIPS is the interphase momentum transfer coefficient. In the following, CFIPS took the values  $10^6$ ,  $10^3$  and  $10^2$ . The results are given in Figure 6. These show the volume fraction contour plots for (a)  $CFIPS = 10^6$ , (b)  $CFIPS = 10^3$  and (c)  $CFIPS = 10^2$  at 0.2s intervals from 0 to 1.6s. At  $t = 0s$ , the bed is stationary. Note that the initial disturbance is hardly discernible at the surface of the sand bed.

As the water flows in, the bed expands becoming dilute very quickly in the lower regions of the domain. In all three cases a bubble forms and gradually grows with time.

Changing the CFIPS values from  $10^6$  to  $10^3$  did not have much influence on the results. However for  $CFIPS = 10^2$ , a considerable difference is noted with the heavier phase moving slower up the channel due to a reduced momentum transfer from the lighter phase. Also a part of the heavier phase remains undisturbed in the lower region of the calculation domain.

### 5.3.2 The Effect of Viscosity

The relationship between the shear stress and the rate of strain for two phase mixtures is not linear. It depends on the heavier phase volume fraction,  $R_2$ . In the present calculation the following relationship (Ref. 12) was used:-

$$\mu = \mu_f \exp [k R_2] \quad (5.4)$$

where

$$k = 2.5 + \frac{14\phi}{d^{0.5}}$$

where

$d$  is the diameter of the particles in microns

and

$\phi$  is the shape factor which is equal to unity for spherical particles

For the present system,  $k = 3.9$ . However, changing the value of  $k$  was found to appreciably affect the results of the calculation. In the following,  $k$  took the values 3.9, 10 and 15.

The results are given in Figure 7. These show the volume fraction contour plots for (a)  $k = 3.9$  (b)  $k = 10$  and (c)  $k = 15$ , when CFIPS =  $10^3$ .

As the water flows in, the bed expands becoming dilute very quickly in the lower region of the domain. For the higher values of  $k$ , a more pronounced bubble is formed with a velocity recirculation region appearing near the wall at later times.

It should be noted that the results shown here are not grid independent. A further increase in the number of cells especially in the radial direction will affect the results. Improving the accuracy of the results is however, not thought to be worthwhile in this part of the study.

### 5.3.3 The Effect of the Wall

The wall shear stress is given by:-

$$\tau_w = \mu \text{ grad } V$$

Since the viscosity,  $\mu$  features in the wall shear stress expression, it was decided to study the isolated effect of the wall. A wall coefficient,  $C$ , was introduced to give:-

$$\tau_w = C\mu \text{ grad } V \quad (5.5)$$

Keeping  $\mu$  constant,  $C$  was given the values 1 and 10.

The results are given in Figure 8. These show the volume fraction contour plots for (a)  $C = 1$  and  $k = 3.9$ , (b)  $C = 10$  and  $k = 3.9$  and (c)  $C = 10$  and  $k = 10$  when  $CFIPS = 10^3$ .

As the water flows in, the bed expands becoming dilute quite quickly. A bubble forms quicker when  $C = 10$  but at later times it can be seen that the effect of the wall is only local. Increasing  $k$  to 10 can be seen not to affect the results appreciably.

#### 5.3.4 Conclusions

Preliminary calculations have established that unless an initial disturbance is specified in the calculations, a bubble will not form. With a small initial disturbance, a parametric study has been conducted.

The results from the study have shown that interphase friction and the 'mixture' viscosity specification are important to the formation and behaviour of the bubble. The effect of the wall was seen to be local.

#### 5.4 The Prediction of the Experiment with a Tilted Interface

The experiment with a tilted interface has been simulated as a two-dimensional two-phase problem. The continuity and momentum conservation equations for each of the phases (see Section 5.1)

have been solved using PHOENICS. The interphase friction description given in equation 5.3 was used with CFIPS =  $10^3$ . The viscosity as given in equation 5.4 was used with  $k = 10$ . The effect of the front, back and two side walls were taken into account with the constant C in equation 5.5 set equal to 1.

The rate of expansion of the part-fixed moving grid corresponded to the mass flow rate into the channel such that the water level in the experiment coincided with the moving boundary of the grid at all times. The grid consisted of 30 cells in the lateral direction and 60 cells in the axial direction. The time step used was 0.005 seconds.

The experimental observations alongside the volume fraction ( $R_2$ ) contour plots and the light and heavy phase velocities ( $W_1$  and  $W_2$ ) are shown in Figure 9. At  $t = 0s$ , the initially tilted interface can be clearly seen. As the water enters the domain from the back, the shallower left-hand side of the bed is accelerated at a faster rate. At  $t = 0.4$  and  $0.6s$ , the experiment shows a bigger 'bulge' believed to be due to three-dimensional effects in the plane perpendicular to the paper. At  $t = 0.8s$ , the bubble appearing in the experiments is seen in the channel. The bubble continues to grow and velocity recirculation regions due to a Kelvin-Helmholtz instability can be seen to have started to form at  $t = 1.0s$ . These continue to grow at  $t = 1.2s$  while the leading edge of the bubble moves further up the channel. The mushroom shape appearing in the experiment at  $t = 1.2s$  appears in the calculations at  $t = 1.4s$ . This continues to move up the channel at  $t = 1.6s$ .

### 5.5 DISCUSSION

The model has predicted in the experiment the initial uneven acceleration of the different parts of the bed, the formation and growth of the bubble and the velocity recirculation regions that appear. It has however overestimated the rate at which the sand moves up the channel as a whole. This is believed to be due to the somewhat simple relationships used for the effective viscosity and the interphase friction.

It should be emphasised that the results obtained here have not been tested for grid independence. In the author's experience with this calcualtion, the refinement of the grid is important especially in the radial direction.

Finally, it should be said that there is a possibility that an oversimplification has been committed in treating the problem as two-dimensional. Although a three-dimensional calcualtion can be carried out, the effort involved cannot be justified for the relatively small improvement that this would make.

### 5.6 CONCLUSIONS

From this part of the work, the following conclusions can be drawn:-

1. The experiment described here has shown that when a lighter continuous phase accelerates through a heavier one, small non-uniformities grow into large ones due to the Rayleigh-Taylor Instability.
2. Despite the absence of combustion from the experiment, it

simulates the hydrodynamics of the gun-barrel situation specifically with regard to the acceleration of a light fluid through a heavier one.

3. The two-phase numerical model employed has predicted fairly well the Rayleigh-Taylor Instability. The discrepancies between the predictions and the experimental observations are attributed to uncertainties about the inter-phase friction and effective-viscosity laws which have been used.
4. The quality of the agreement between predictions and the observations gives credibility to the predictions which the same computational procedure produces when it is applied to a gun-barrel simulation involving combustion.

The remaining part of this report dedicates itself to the prediction of the gun-barrel situation especially with regard to the growth of large non-uniformities from smaller ones.

## 6. Numerical Simulation of the Gun-Barrel Situation

### 6.1 Introduction

It has been demonstrated above that the acceleration of a fluid containing a dispersed heavier phase leads to large bubble formation, a consequence of the Rayleigh-Taylor Instability. In guns, initial particle packing non-uniformities or those that develop as the ignitor discharges the hot gas into the propellant bed may prove to be the source of volume fraction discontinuities resulting from the Rayleigh-Taylor instability. The objective in

this part of the work is to establish whether low-particle-density regions or 'bubbles' can occur under conditions which are true of guns.

If R-T bubbles do occur in guns, then irregularities in the rate of combustion of the propellant particles can be expected. Also, the bubbles would appreciably affect the radial velocities of the unburnt or partly burned particles thus influencing the heat transfer to and erosion of the barrel walls.

In what follows, two calculations are presented. The first simulates a gun-like situation where particles contained in a cylindrical domain ignite, which raises the pressure within the domain causing it to expand. The expanding domain simulates the movement of the projectile in guns. The results from such a calculation are described and discussed.

The second calculation is identical to the first except that a small non-uniformity in the volume fraction distribution is introduced. The results from this calculation are described and compared with the previous calculation especially with regard to the effect that the initial non-uniformity has had.

It is worth noting that the calculations presented here do not provide quantitative results of the gun barrel problem. They are aimed more at demonstrating that, with the acceleration provided by the movement of the projectile, the non-uniformities that may be present grow in size.

## 6.2 The Physical Problem

The basic features of the gun barrel are outlined in Figure 10. A cylindrical domain is considered, enclosed by the gun barrel and the base of the projectile, and containing a solid propellant and a gas. The solid propellant is assumed to be spherical particles.

Ignition is provided by the inflow of hot gases at the base of the domain. The gas is forced into the propellant bed which causes a compaction of the granular bed near the entrance region and also heats up the nearby granular propellants to ignition. The ignited propellants give off more hot gases which are pushed forward by the pressure gradient to ignite more propellants. Thus a pressure gradient is created inside the combustion chamber and the accelerated gaseous products cause the projectile to move.

The modelling of such unsteady two-phase flow phenomena requires the solution of the unsteady two-phase gas dynamic equations as well as the utilisation of associated empirical correlations for interphase friction and heat transfer coefficients and burning rate laws for the rate of interphase mass transfer.

## 6.3 The Dependent and Independent Variables

The dependent variables of the problems are: the velocities of the gas and particles in the axial and radial directions,  $w_1$ ,  $w_2$ ,  $v_1$  and  $v_2$ ; gas and particle volume fractions  $R_1$  and  $R_2$ ; and enthalpies of gas and particles  $h_1$  and  $h_2$ .

The independent variables are: the axial and radial distances  $z$  and  $r$ ; and the time  $t$ .

#### 6.4 The Partial Differential Equations

The following set of governing equations describe the change of mass, momentum and energy for each of the gas and solid phases.

##### 6.4.1 The Mass Conservation Equation

Gas Phase

$$\frac{\partial}{\partial t} (\rho_1 R_1) + \frac{\partial}{\partial z} (\rho_1 R_1 w_1) + \frac{1}{r} \frac{\partial}{\partial r} (\rho_1 R_1 r v_1) = \dot{m}_{21} \quad (6.1)$$

Particle Phase

$$\frac{\partial}{\partial t} (\rho_2 R_2) + \frac{\partial}{\partial z} (\rho_2 R_2 w_2) + \frac{1}{r} \frac{\partial}{\partial r} (\rho_2 R_2 r v_2) = -\dot{m}_{21} \quad (6.2)$$

where

$\rho_1$  and  $\rho_2$  are the densities of the gas and particle respectively

$v_1$ ,  $v_2$ ,  $w_1$  and  $w_2$  are the velocities of the gas and particle in the radial and axial directions

and

$\dot{m}_{21}$  is the rate of mass transfer per unit volume from the solid phase to the gaseous phase due to gasification of the solid particles

The volumetric fractions are related by the space-sharing equation:-

$$R_1 + R_2 = 1 \quad (6.3)$$

#### 6.4.2 The Conservation of Momentum Equations

The momentum equations for a transient two-phase flow are:-

$$\begin{aligned} \frac{\partial}{\partial t} (\rho_i R_i \phi) + \frac{1}{r} \frac{\partial}{\partial r} (r R_i \rho_i v_i \phi) + \frac{\partial}{\partial z} (R_i \rho_i w_i \phi) \\ = - \frac{1}{r} \frac{\partial}{\partial r} (r R_i \Gamma \phi) + \frac{\partial}{\partial z} (R_i \Gamma \phi) + S \phi \quad (6.4) \end{aligned}$$

where

$\phi$  stands for  $v_1, v_2, w_1$  and  $w_2$ ;

$\Gamma$  is the diffusion coefficient

$S$  represents source/sink of momentum due to pressure gradients, gravitational forces etc...

and the subscript  $i$  refers to the phase in question i.e. gaseous or solid.

For the application of the model considered in this part of the work, diffusion effects are considered negligible ( $\Gamma = 0$ ).

The source terms on the RHS of equation 6.4 are given in Table 1. The effect of the wall has been neglected. Note that the pressure gradient term is written as  $R \text{ grad } p$  as opposed to  $\text{grad } (p R)$ . The form used in the present work is the correct one (Ref. 13).

In the present formulation, the two phases share the same pressure. However, an additional 'intergranular force' term,  $\text{grad } (R_2 \tau)$ , appears in the solid phase equation. This describes the extra stress,  $\tau$ , sustained by the solid phase as its volume fraction approaches the physically attainable limit. This

intergranular stress is a function of the volume fraction  $R_2$ .

The  $m_{21} \langle v_i \rangle$  terms describe the rate of change of momentum due to the motion of the gasifying particles.

#### 6.4.3 The Conservation of Energy Equations

##### Gas Phase

$$\begin{aligned} \frac{\partial}{\partial t} [R_1 (\rho_1 h_1 - p)] + \frac{1}{r} \frac{\partial}{\partial r} (r R_1 \rho_1 v_1 h_1) + \frac{\partial}{\partial z} (\rho_1 R_1 w_1 h_1) \\ = C_f (v_2 - v_1) v_2 + C_f (w_2 - w_1) w_2 \\ - \dot{q}_{12} + \dot{m}_{21} (h_s + v_1^2/2 + w_1^2/2) \\ - p \frac{\partial R_1}{\partial t} \end{aligned} \quad (6.5)$$

##### Particle Phase

$$\begin{aligned} \frac{\partial}{\partial t} [R_2 (\rho_2 h_2 - p)] + \frac{1}{r} \frac{\partial}{\partial r} (r R_2 \rho_2 v_2 h_2) + \frac{\partial}{\partial z} (\rho_2 R_2 w_2 h_2) \\ = C_f (v_1 - v_2) v_1 + C_f (w_1 - w_2) w_1 \\ + \dot{q}_{12} - \dot{m}_{21} (h_s + v_2^2/2 + w_2^2/2) \\ - p \frac{\partial R_2}{\partial t} \end{aligned} \quad (6.6)$$

where

$$p = p + \tau$$

$\dot{q}_{12}$  is the rate of heat transfer from the gas to the particles

$$h_s = h_2 + h_c$$

where

$h_c$  is the heat of combustion of the solid particles.

In the above, the rate of heat transfer within the solid phase by conduction has been neglected. The rate of heat transfer to the gun barrel wall has also been neglected.

Equation 6.1 to 6.6 form a system of nine coupled, non-

linear, partial differential equations. These have been solved using the PHOENICS computer code.

### 6.5 Auxilliary Relations

To complete the mathematical specification of the problem constitutive relations are needed. Some of the relations presented below are simple and need improvement if accurate results are to be obtained. These however are not essential to the Rayleigh-Taylor problem.

#### 6.5.1 Equation of State

The equation of state for a perfect gas undergoing an isentropic process was used. This is given by:-

$$p e^{-\alpha} = \text{const.} \quad (6.7)$$

A more representative equation of state would be the Nobel-Abel or Clausius equation (Ref. 14) which takes into account the molecular volume.

#### 6.5.2 The Intergranular Stress

A granular packed bed under compressive load can be further compacted. A measure of this compaction is the volume fraction of the heavy phase,  $R_2$ . There is however, a limiting maximum compaction depending on the particle shape, properties and size distribution. In the case of unisized, incompressible and spherical solids, the maximum compaction corresponds to approximately  $R_2 = 0.75$ . If the particles are of different sizes in the bed, higher compaction is possible.

Under compressive loads, there is a force that resists this compaction. This force, termed the particle-particle or intergranular stress, depends on the stress-strain relation of the lattice which is different from the stress-strain relation of the pure homogeneous solid. In the present model, the effect of the intergranular stress has been ignored but three different relationships can be found in Refs. 14 and 15.

#### 6.5.3 The Interphase Friction Coefficient

The interphase friction force is given by:-

$$F = f | w_1 - w_2 |$$

where  $w$  refers to any velocity component and  $f$  is the interphase friction factor given by

$$f = C_f \rho_2 R_1 R_2 \text{ Vol} \quad (6.8)$$

where  $\text{Vol}$  is the control cell volume.

In the present model, equation 6.8 has been used. Empirical correlations are given in Refs. 16 and 17.

#### 6.5.4 The Particle Burning Rate

The governing equations have a very important source term,  $m_{21}$ , which describes the rate at which the gas phase mass is generated from the combustion of the solid propellant particles. The rate of mass generation is a function of the particle burning rate which is determined by the rate at which the solid gasifies at its burning surface. In general, the burning rate depends on the proportion of the propellant particles, the initial temperature and most importantly the pressure. The burning rate law is written as:-

$$b = \epsilon \left( \frac{p}{p_{atm}} \right)^n \quad (6.9)$$

where

$p_{atm}$  is the atmospheric pressure

and

$\epsilon$  and  $n$  are constants.

The production rate of gases from the solid particles is therefore given by:-

$$\dot{m}_{21} = b A_s \quad (6.10)$$

where

$A_s$  is the total surface area of particles in a control cell

calculated for spherical particles from

$$A_s = \frac{6 R_2 \text{ Vol}}{D_0}$$

where

Vol is the control cell volume

and

$D_0$  is the initial diameter of unburnt particles

It should be noted that the present calculations do not account for the reduction in particle size due to combustion. Consequently, the rate of gas generation is therefore overestimated.

An important improvement to the present model would employ the 'shadow' method for particle size calculation (Ref. 18).

#### 6.5.5 Ignition Criterion

The particle is assumed to ignite when its surface temperature reaches a specified value i.e.

$$\begin{aligned}\dot{b} &= 0 & T_s &< T_{\text{ignition}} \\ \dot{b} &= \epsilon \left( \frac{p}{p_{\text{atm}}} \right)^n & T_s &> T_{\text{ignition}}\end{aligned}\quad (6.11)$$

The particle surface temperature is determined from equation 6.15 below.

#### 6.5.6 The Interphase Heat Transfer Coefficients

Although the equations solved for the transport of heat between the gas and particle phases are those of the phase enthalpies (equations 6.5 and 6.6), it is convenient to think in terms of the temperatures  $T_1$  and  $T_2$  by introducing the specific heats  $C_1$  and  $C_2$  for the gas and particle phases respectively. For simplicity,  $C_1$  and  $C_2$  are assumed equal ( $= C$ ).

Central to the following treatment is the concept of an interface between the two phases with temperature  $T_s$ . Then

$$\dot{q}_{1s} = a_1 (T_1 - T_s) \quad (6.12)$$

$$\dot{q}_{s2} = a_2 (T_s - T_2) \quad (6.13)$$

where the subscripts 1, 2 and s refer to the gas, solid and the interface respectively.

$\dot{q}$  is the rate of heat transfer and  $a_1$  and  $a_2$  are the heat transfer coefficients multiplied by the interface area through which the transfer occurs.

An energy balance over the control volume enclosing the interface yields:

heat coming into the control volume

$$= \dot{q}_{1s} + \dot{m}_{21} CT_2$$

heat going out of the control volume

$$= \dot{q}_{s2} + \dot{m}_{21} CT_s$$

$$\text{generation} = \dot{m}_{21} h_c$$

where

$\dot{m}_{21}$  is given in equations 6.10 and 6.11

and

$h_c$  is the heat of combustion of the solid particles

Therefore

$$\dot{q}_{s2} - \dot{q}_{1s} = \dot{m}_{21} [h_c - C(T_s - T_2)] \quad (6.14)$$

Combining equations 6.12, 6.13 and 6.14 yields

$$T_s = [a_2 T_2 + a_1 T_1 + \dot{m}_{21} (h_c + CT_2)]/A \quad (6.15)$$

$$\dot{q}_{1s} = a_1/A [a_2(T_1 - T_2) + \dot{m}_{21} C(T_1 - T_2) - \dot{m}_{21} h_c]$$

$$\dot{q}_{s2} = a_2/A [a_1(T_1 - T_2) + \dot{m}_{21} h_c]$$

where

$$A = a_1 + a_2 + \dot{m}_{21} C$$

The heat transfer coefficient per unit area,  $a_1$ , is calculated from the Denton (Ref. 19) correlation as modified by Eckert and Drake (Ref. 20) given by:-

$$Nu = \frac{a_1 D}{k_1} = 0.4 Re^{0.7} Pr^{0.3}$$

where

$k_1$  is the thermal conductivity of the gas

$D$  is the particle diameter

$Re$  is the Reynolds Number given by:-

$$Re = \rho_1 (W_1 - W_2) R_1 D / \mu_1$$

and

Pr is the Prandtl Number given by:-

$$Pr = \mu_1 C/k_1$$

#### 6.5.7 The Movement of the Projectile

The projectile velocity and acceleration were calculated at every time step from the computed force,  $F$ , acting on its base.

$$F = (p_f - p_b)A$$

where

$p_f$  = projectile frictional pressure

$p_b$  = calculated pressure at the base of the projectile

and

$A$  = projectile cross-sectional area

#### 6.6 The Problem Considered

The problem considered is that of predicting the time-dependent two-phase two-dimensional heat transfer and combustion processes occurring in a gun barrel as illustrated in Figure 10. Table 2 summarizes the input data used and the initial conditions employed.

At  $t = 0s$ , hot gases flow into the domain. The heat transfer to the particles raises their surface temperature until the ignition temperature is reached initiating combustion. Further hot gases are produced as a result of combustion and the pressure builds up inside the domain. The temperature also increases igniting more particles. When the pressure is sufficiently high, the projectile starts to move.

Two calculations are presented below. The first computes

variations with time along the axial direction only. In the second calculation, a non-uniformity in the volume fraction distribution is introduced. The results from the two calculations are compared to demonstrate the effect of the initial non-uniformity on the results.

#### 6.7 Computational Details

The gun barrel shown in Figure 10 is divided into a number of annular cells in the axial and radial directions. An example is given in Figure 11 which shows two cells in the axial z direction and three cells in the radial y direction.

A numerical test was performed to establish the dependence of the results on the number of cells in the axial direction. In a 1D calculation, and for a fixed time interval of 0.04ms, the number of cells was varied from ten to thirty keeping all other properties unchanged. The dependence of the pressure on the number of cells is shown in Figure 12. It can be seen that little accuracy can be gained from increasing the number of axial cells beyond thirty. In the following calculations, 30 and 16 cells were used in the axial and radial directions. The time interval used was 0.02ms.

Following the projectile movement, the grid was allowed to expand in the axial direction at every time step subject to the conditions outlined in section 6.5.7 above. The lower twenty cells corresponding to the first 0.13m from the bottom of the barrel were not allowed to move.

## 6.8 RESULTS

### 6.8.1 Simulation of the gun situation

The results from are shown in Figures 13 to 17. The axial distribution histories for the pressure, gas and particle velocities, particle volume fraction and temperature are given.

In figure 13, the axial pressure distribution is shown at  $t=0.5, 1.5, 2.5, 3.5, 4.5, 5.5$  and  $6.5\text{ms}$ . At  $t=0.5\text{ms}$ , the pressure near the base of the barrel rises sharply due to the inflow of hot gases which ignite the particles in this region. A steep pressure gradient is obtained which diminishes with time. The pressure builds up with time and at  $t=2.5\text{ms}$  it exceeds  $1 \text{ M Pa}$  the point at which the projectile starts to move. Despite the movement of the projectile (at  $t=2.16\text{ms}$ ) the pressure continues to rise due to particle gasification until it reaches a maximum of around  $20 \text{ M Pa}$  at  $t=6.5\text{ms}$ .

Figures 14 and 15 show the gas and particle axial velocity distributions at the same times as those for the pressure. A peak is observed in both the gas and particle profiles up to  $t=2.5\text{ms}$  driven by the pressure gradient. Beyond  $t=2.5\text{ms}$ , a peak in the gas velocity profile is obtained behind the projectile as it drags the gas with it. A maximum gas velocity of about  $300\text{m/s}$  is obtained at  $t=6.5\text{ms}$ . The particle velocity is much lower due to the higher inertia that the particles possess. A maximum particle velocity of about  $130\text{m/s}$  is obtained at  $t=6.5\text{ms}$ .

The particle volume fraction ( $R2$ ) distribution history is shown in figure 16. Near the base of the barrel, the  $R2$  values decrease quite rapidly due to the burning of the particles and their forward motion as they are carried by the gas. The effect

of the latter causes a compaction of the particles in other regions of the barrel. This is clearly seen in figure 16 where the R2 values increase beyond the initial value of 0.5. This effect is however exaggerated here due to the neglect of the intergranular stress which acts to resist this compaction (see section 6.5.2). Near the base of the projectile, the sharp decrease in the R2 values for  $t > 2.5\text{ms}$  is caused by the movement of the projectile.

Figure 17 gives the gas temperature,  $T_1$ , axial distribution history. At all times near the bottom of the barrel,  $T_1$  remains at 2000K which is the temperature of the injected gas specified as an initial condition. This temperature, however, decays rapidly with axial distance downstream. With time,  $T_1$  builds up gradually in the top part of the barrel due to heat transfer by convection combined with combustion - generated heat. The particle temperature distribution history follows closely that for  $T_1$  due to the high heat transfer coefficient,  $a_2$ , which was used.

Finally, the projectile velocity and acceleration are shown in Figure 18. The projectile starts moving at  $t = 2.16\text{ms}$  and accelerates rapidly to about  $12000 \text{ m/s}^2$  at  $t = 6 \text{ ms}$  after which the acceleration decreases. The velocity at  $t = 6\text{ms}$  is about 75m/s. In 6.5ms, the acceleration of the projectile produces a 73.5% expansion in the length of the domain.

### 6.8.2 The effect of an initial non-uniformity

An initial volume fraction non-uniformity was introduced in the calculation. This non-uniformity consisted of a cell in which the particle volume fraction,  $R_2$ , was reduced from 0.5 to 0.1 while its two neighbouring cells in the radial direction had  $R_2 = 0.7$ . This disturbance occupied only one cell in the axial  $Z$  direction at  $Z/L = 0.33$  and  $r/R = 0.64$ . Since the volume of the computational cells is everywhere constant, the total amount of propellant mass is therefore unchanged. With the exception of the three above mentioned cells, the  $R_2$  values were everywhere equal to 0.5.

The effect of this non-uniformity on the pressure and temperature has not been significant. The pressure and temperature distribution histories are very similar to figures 13 and 17 with no significant variations in the radial direction.

The gas velocity axial distribution history given in figure 19 shows a sudden increase in the gas velocity at  $t = 0.5\text{ms}$  and  $Z/L = 0.33$ . This coincides in position with the initial non-uniformity and is typical of the RTI. For the RTI accelerates unevenly the parts of the flow which contain volume fraction non-uniformities. The acceleration for  $t < 2.5\text{ms}$  is not provided by the movement of the projectile (as it has not yet started to move) but is due to the pressure gradient within the barrel (see figure 13).

The uneven axial gas velocity distribution is evident throughout the calculation although figure 19 does not show it. In figure 20, the radial gas velocity distribution at (a)  $Z/L = 0.33$  and (b)  $Z/L = 0.88$  is given. At  $Z/L = 0.33$  the non-uniform

gas velocity is seen to be at its greatest at  $t = 0.5\text{ms}$  after which it diminishes due to the forward movement of the volume fraction non-uniformity and the reduction in its magnitude due to the effects of compaction. At  $Z/L = 0.88$  (figure 20 (b)), the uneven velocity profiles are only seen at later times.

The volume fraction axial distribution history is shown in figure 21. For clarity of presentation, the  $R_2$  profiles have been given in figure 21 (a) at  $t=0.5, 1.5$  and  $2.5\text{ms}$  and in figure 21 (b) at  $t=3.5, 4.5, 5.5$  and  $6.5\text{ms}$ . At  $t=0.5\text{ms}$ , the volume fraction non-uniformity is seen to extend from  $Z/L = 0.35$  to  $Z/L = 0.45$  thus occupying about 10% of the domain length. Its magnitude however ranges between  $R_2 = 0.15$  to  $0.5$ . At subsequent times, the magnitude of the non-uniformity is seen to diminish but it grows in size. For at  $t=4.5\text{ms}$  (figure 21 (b)) the non-uniformity occupies about 30% event though its magnitude ranges between  $R_2=0.7$  and  $0.8$ . The decrease in the magnitude of the non-uniformity is due to the effects of compaction but the increase in its size is due to RTI.

The significance of the RTI can be appreciated when comparing the volume fraction profiles from this calculation with the corresponding ones in the absence of the initial non-uniformity. This is done in figure 22 for (a)  $t=0.5\text{ms}$ , (b)  $t=2.5\text{ms}$ , (c)  $t=4.5\text{ms}$  and (d)  $t=6.5\text{ms}$ . The increase in the size of the non-uniformity can be clearly seen although at  $t=6.5\text{ms}$  it is affected by the movement of the projectile.

The volume fraction radial profiles at  $Z/L = 0.33$  and  $Z/L = 0.88$  are given in figure 23 (a) and (b). The non-uniformity is

seen not to grow in the radial direction.

#### 6.8.3 Discussion

The calculation presented in section 6.8.1 has produced realistic results from a simplified model for the combustion of propellant particles in a gun barrel. The inflow of the hot gases causes the particles to ignite raising the pressure and temperature, thus igniting more particles and causing the projectile to eventually move. The inflow of hot gases pushes the particles away from the injection region and causes them to compact everywhere else. The neglect of intergranular stress from these calculations has given rise to high compaction and subsequently high volume fraction values.

The introduction of a small non-uniformity has not affected the pressure nor the temperature significantly. But the initial volume fraction non-uniformity was seen to increase in size as it moves along the barrel despite a decrease in its magnitude. The magnitude of the non-uniformity is believed to have been strongly affected by the compaction of the particles which has been exaggerated through the neglect of intergranular stress. But the RTI is still evident even though it is superimposed on top of other effects. A sketch of the author's view of what happens is given in figure 24.

#### 6.9 Conclusions

From this part of the work, the following conclusions can be drawn.

1. The simulation of a simplified gun barrel has produced realistic results using a numerical procedure which was previously shown to predict the RTI satisfactorily.
2. A calculation, in which a small initial non-uniformity in the particle volume fraction has been introduced, demonstrated that these do grow as a consequence of the Rayleigh-Taylor Instability.
3. The growth of the non-uniformity and the common features that this calculation has with the gun barrel situation gives credibility to the notion that the possibility of RTI in guns deserves attention.

#### 7. Future Work

The model used for simulating the combustion within the gun barrel can be improved to provide realistic predictions. These improvements would involve better expressions for the equation of state, the interphase friction and the intergranular stress. A particle size calculation should also be introduced. Recommended expressions have been given in section 6.5.

Variable	Source Terms
$w_1$	$R_1(\rho_1 g - \frac{\partial p}{\partial z}) + c_f (w_2 - w_1) + \dot{m}_{21} w_2$
$w_2$	$R_2(\rho_2 g - \frac{\partial p}{\partial z}) - c_f (w_2 - w_1) - \dot{m}_{21} w_2 - \frac{\partial R_2 \tau}{\partial z}$
$v_1$	$R_1(\rho_1 g - \frac{\partial p}{\partial y}) + c_f (v_2 - v_1) + \dot{m}_{21} v_2$
$v_2$	$R_2(\rho_2 g - \frac{\partial p}{\partial y}) - c_f (v_2 - v_1) - \dot{m}_{21} v_2 - \frac{\partial R_2 \tau}{\partial y}$

where  $g$  is the gravitational acceleration:  
 $\rho$  is the pressure:  $c_f$  is the interphase  
friction coefficient and  $\tau$  is the inter-  
granular stress.

TABLE 1: The Source terms in the momentum equations

Parameter	Value
<u>Physical Properties</u>	
Propellant density	1500 kg/m <sup>3</sup>
Specific heat ratio of gas, $\alpha$	1.4
Ignition temperature	400K
Chemical energy of propellant, $h_c$	4 MJ/kg
Specific heat of gas and particle, $C_f$	2000 J/kg K
Mass in flow rate from ignitor	40 kg/s m <sup>2</sup>
Temperature of gas from ignitor	2000K
<u>Constitutive Relations</u>	
Propellant burning rate proportionality constant, $\epsilon$	0.2 kg/m <sup>2</sup> s
Propellant burning rate index, $n$	0.9
Interphase friction parameter, $C_f$ (eqn. 6.9)	100
Interphase heat transfer parameter on particle side, $a_2$	20W/K
<u>Initial Conditions</u>	
Pressure	$1 \times 10^5$ N/m <sup>2</sup>
Bulk temperature of solid particles	294K
Temperature of gas	294K
Volume fraction of solid, $R_2$	0.5
Velocities of gas and particles, $v_1$ , $v_2$ , $w_1$ and $w_2$	0.0ms
Particle diameter	300 $\mu$ m
<u>Other Input</u>	
Projectile frictional pressure	1M Pa
Projectile mass	2kg

TABLE 2:  
Input data used in the calculations (source Refs. 14 and 15)

## 8. MOMENCLATURE

$a_1, a_2$	heat transfer parameters for the gas and particles respectively (see equations 6.12 and 6.13)
$A$	projectile cross-sectional area
$A_s$	total surface area in a control cell
$At$	Atwood Number
$b$	burning rate of particles
$c_1, c_2$	specific heats of gas and particle respectively
$c_f$	interphase friction coefficient
CFIPS	interphase momentum transfer coefficient (see equation 5.3)
$d_0$	initial particle diameter
$g$	acceleration due to gravity
$h$	enthalpy
$h_c$	heat of combustion
$k$	thermal conductivity
$\dot{m}_{21}$	rate of interphase mass transfer
$n$	propellant burning rate index
$Nu$	Nusselt Number
$p$	pressure
$p_b$	pressure at the base of the projectile
$p_f$	projectile frictional pressure
$q$	rate of heat transfer
$r$	radial co-ordinate
$R$	volume fraction
$t$	time
$T$	temperature
$T_{ignition}$	propellant ignition temperature

$T_s$	particle surface temperature
$\langle v \rangle$	Velocity vector
Vol	control cell volume
y	lateral co-ordinate
z	axial co-ordinate

#### Greek Symbols

$\alpha$	specific heat ratio of gas
$\Gamma$	diffusion coefficient
$\epsilon$	propellant burning rate
	proportionality constant
$\lambda$	wavelength
$\mu$	dynamic viscosity
$\rho$	density
$\tau$	intergranular stress
$\tau_w$	wall shear stress

#### Subscripts

1	pertaining to the gas phase
2	pertaining to the solid phase
s	pertaining to the interface

9. REFERENCES

1. FARWAGI, S.M. (1984)  
The behaviour of unstable surfaces - a literature review.  
Imperial College Computational Fluid Dynamics Report.  
CFD/84/6.
2. MELCHER, J.R. and HURWITZ, M. (1967)  
Gradient stabilization of electrohydrodynamically orientated  
liquids.  
J. of Spacecraft and Rockets, Vol. 4, No.7, p.864.
3. ANDREWS, M.J. (1986)  
Turbulent mixing by Rayleigh-Taylor  
Instability  
University of London PhD Thesis  
Imperial College Computational Fluid Dynamics Report.  
CFD/86/10.
4. DALY, B.J. (1969)  
J. Phys. Fluids, Vol. 12, p. 1340.
5. LEWIS, D.J. (1950)  
The instability of liquid surfaces when accelerated in a  
direction perpendicular to their planes.  
Proc. Roy. Soc. (London) A202, p.81.
6. READ, K.I. and YOUNGS, D.L. (1983)  
Experimental investigation of turbulent mixing by Rayleigh-  
Taylor Instability  
AWRE Report No. 011/83.
7. BIRKHOFF, G. and CARTER, D. (1957)  
J. Math and Mech. Vol. 6, No.6, p.769.
8. SPALDING, D.B. (1984)  
PHOENICS 84 - A multi-dimensional multi-phase general  
purpose computer simulator for fluid flow, heat transfer and  
combustion.  
Imperial College Computational Fluid Dynamics Report  
CFD/84/18
9. SPALDING, D.B. (1981)  
A general purpose computer program for multi-dimensional one  
and two-phase flows.  
Mathematics and Computers in Simulation  
North Holland Press, Vol. XXIII, p. 267.
10. SPALDING, D.B. (1982)  
Four lectures on the PHOENICS computer code  
Imperial College Computational Fluid Dynamics Report  
CFD/82/5
11. AWN, A.G.A. (1979)

Numerical modelling of flows with moving interfaces.  
University of London PhD Thesis  
Imperial College Computational Fluid Dynamics Report  
HTS/79/16

12. WALLIS, G.B. (1969)  
One-Dimensional two-phase flow  
McGraw-Hill
13. SPALDING, D.B. (1986)  
Computer Simulation of Chemical Engineering Processes  
Lectures and computer workshops held at Imperial  
College, May 1986.
14. GOKHALE, S.S. and KRIER, H (1982)  
Modelling of unsteady two-phase reactive flow in porous  
beds of propellant.  
Prog. Energy Combust. Sci. Vol. 8, pp. 1-39.
15. MARKATOS, N.C. and KIRKCALDY, D. (1983)  
Analysis and computation of three-dimensional, transient  
flow and combustion through granulated propellants.  
Int. J. Heat and Mass Transfer, Vol. 26.  
No. 7, pp. 1037-1053.
16. ERGUN, S. (1952)  
Fluid flow through packed columns  
Chemical Engineering Progress  
Vol. 48, pp. 89-96.
17. KUC, K.K. and NYDEGGER, C.C. (1978)  
Cold flow resistance measurement and correlation in a  
packed bed of WC-870 spherical propellants.  
Journal of Ballistics, Vol. 2, pp.1-26.
18. SPALDING, D.B. (1982)  
The 'Shadow' method of particle-size calculation in two-  
phase combustion.  
Imperial College Computational Fluid Dynamics Report  
CFD/82/1
19. DENTON, W.H. (1951)  
The heat transfer and flow resistance for fluid flow  
through randomly packed spheres.  
ASME Transactions, p. 370.
20. ECKERT, E.P.G. and DRAKE, E.M. (1972)  
Analysis of heat and mass transfer.  
McGraw Hill.

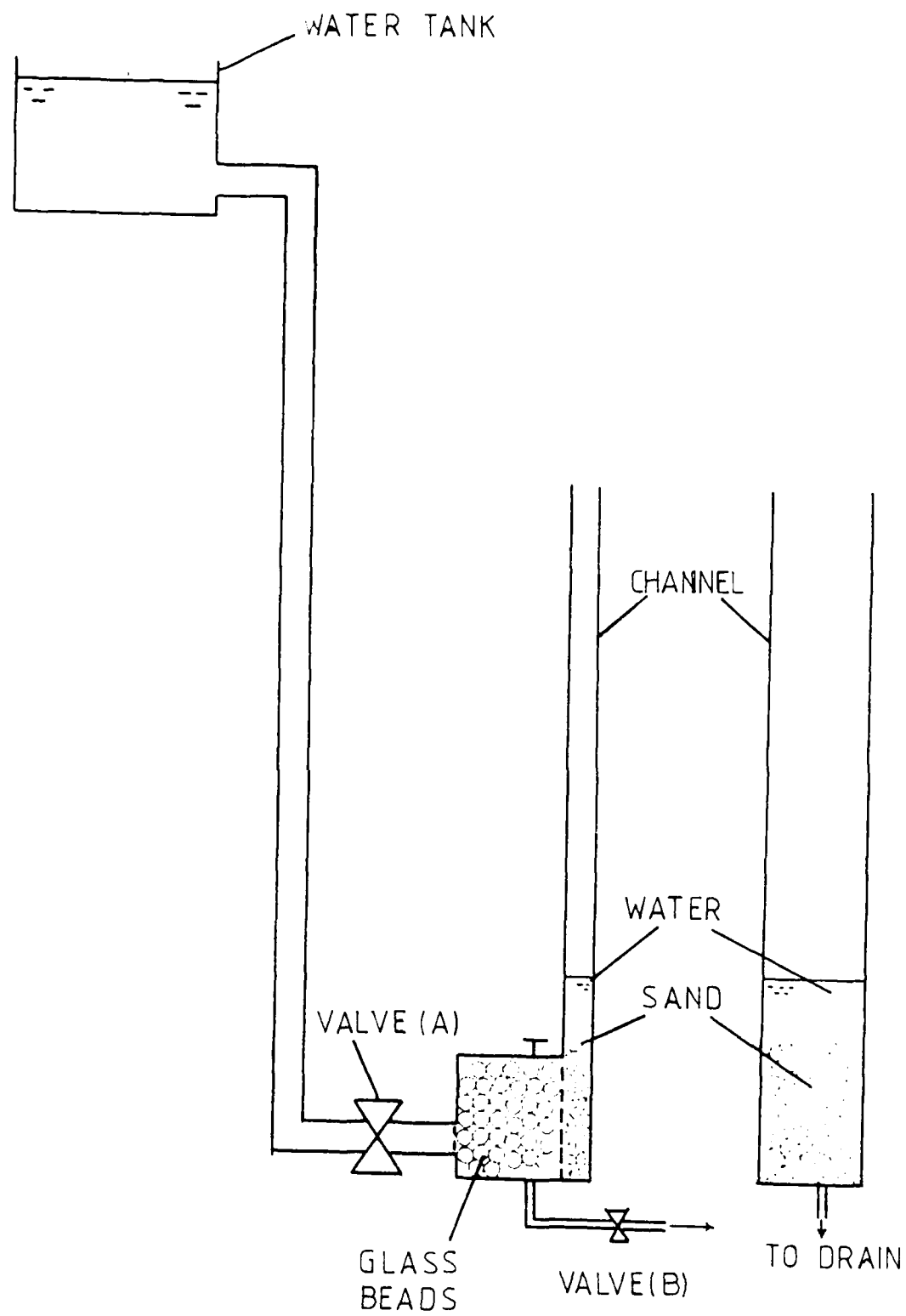


Figure 1 : Schematic diagram of the experimental apparatus used



$t = 0.0 \text{ s}$



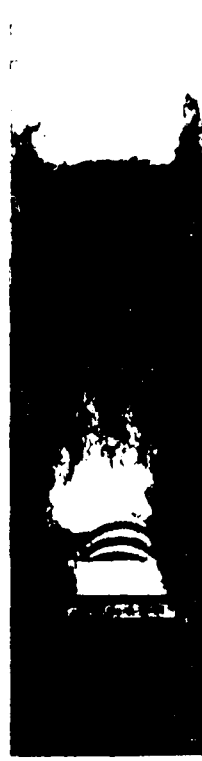
$t = 0.2 \text{ s}$



$t = 0.4 \text{ s}$



$t = 0.6 \text{ s}$



$t = 0.8 \text{ s}$



$t = 1.0 \text{ s}$

Figure 2 : Observations in the experiment with a flat interface



$t = 1.2 \text{ s}$



$t = 1.4 \text{ s}$



$t = 1.6 \text{ s}$

Figure 2 (cont'd) : Observations in the experiment with a flat interface (cont'd)



$t = 0.0 \text{ s}$



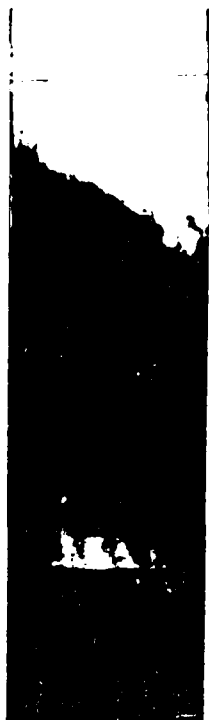
$t = 0.2 \text{ s}$



$t = 0.4 \text{ s}$



$t = 0.6 \text{ s}$



$t = 0.8 \text{ s}$



$t = 1.0 \text{ s}$

Figure 3 : Observations in the experiment with a tilted interface



$t = 1.2 \text{ s}$



$t = 1.4 \text{ s}$



$t = 1.6 \text{ s}$

Figure 3 (cont'd) : Observations in the experiment with  
a tilted interface (cont'd)

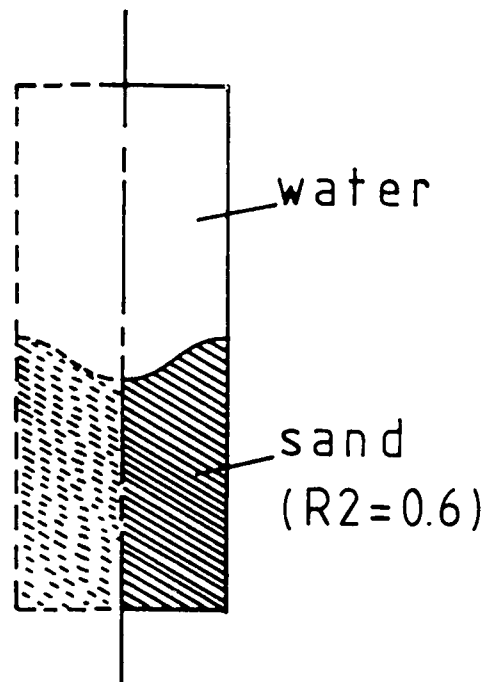


Figure 4 : An exaggerated view of the initial sinusoidal disturbance

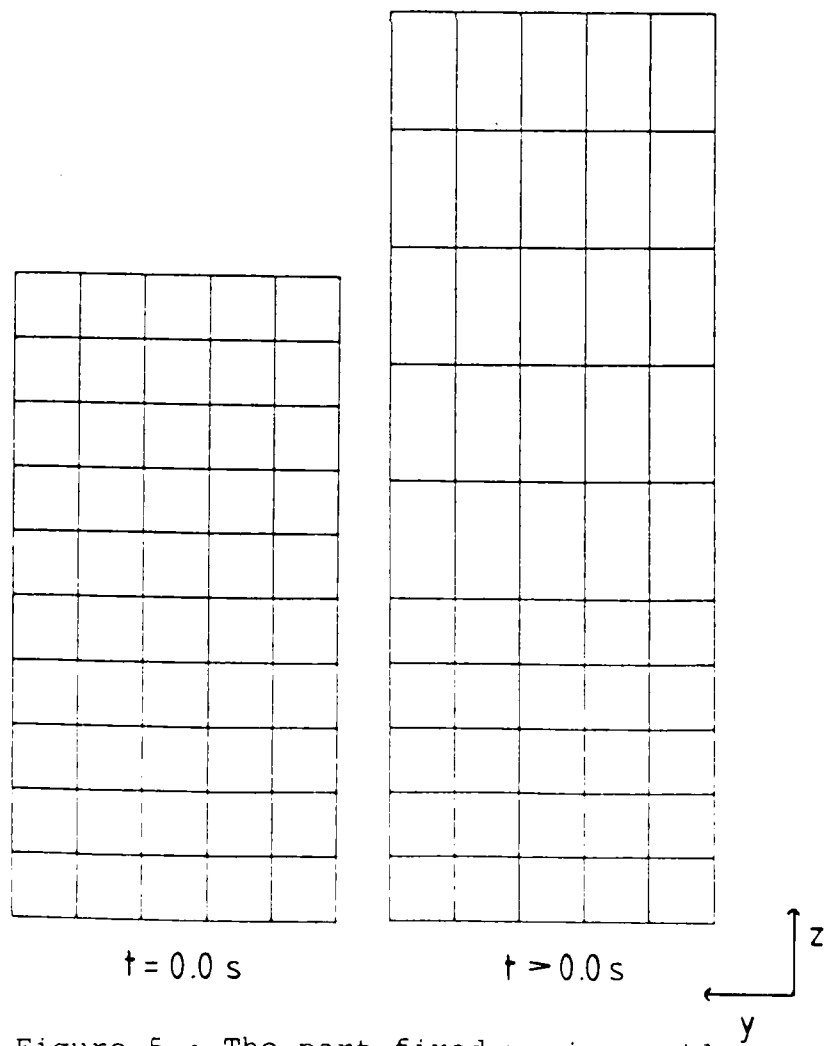
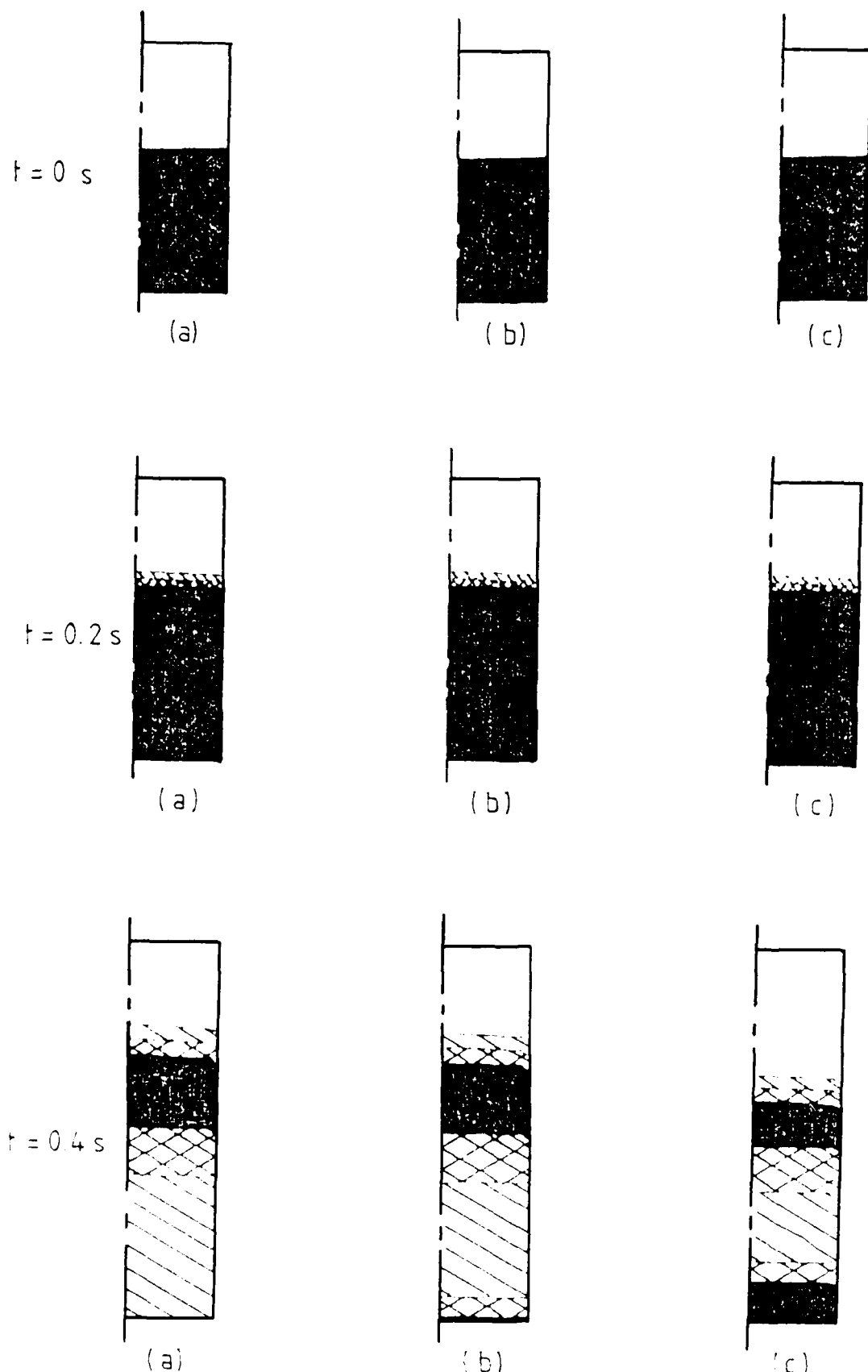


Figure 5 : The part-fixed moving grid



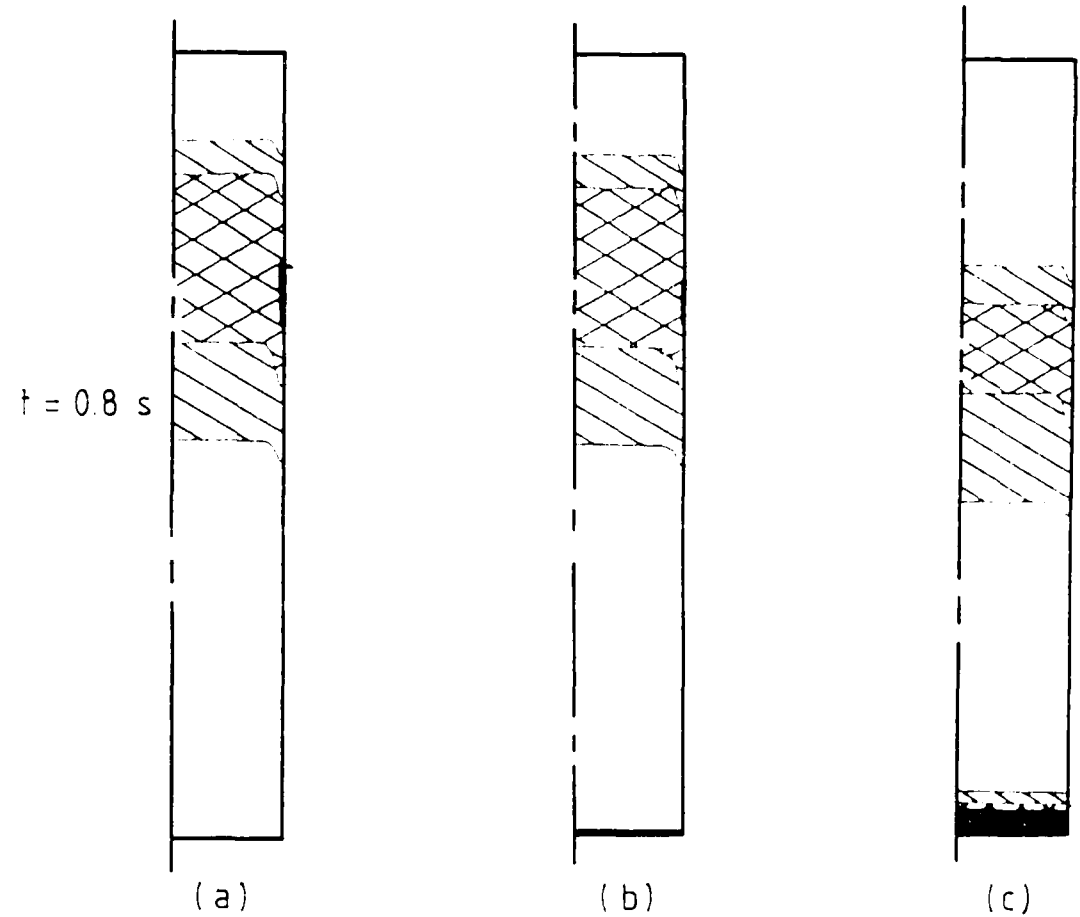
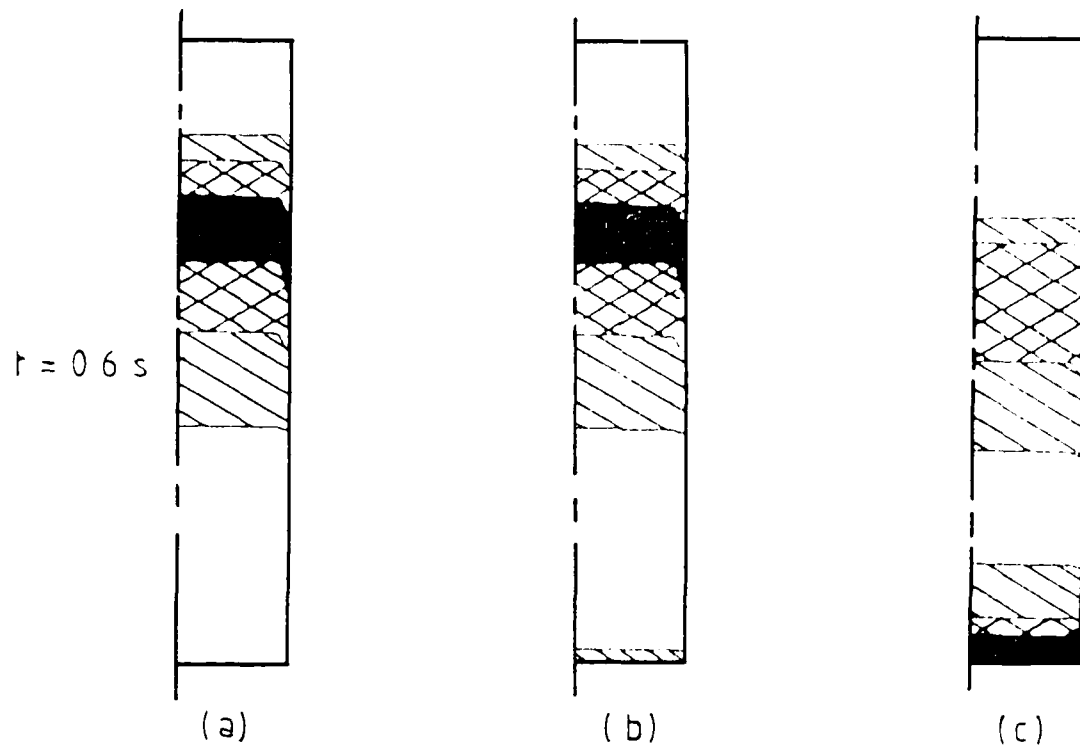


Figure 6 (cont'd) : The effect of CFIPS

(a)  $\text{CFIPS} = 10^6$   
 (b)  $\text{CFIPS} = 10^3$   
 (c)  $\text{CFIPS} = 10^2$

	$R_2 > 0.35$
	$0.35 > R_2 > 0.25$
	$0.25 > R_2 > 0.15$

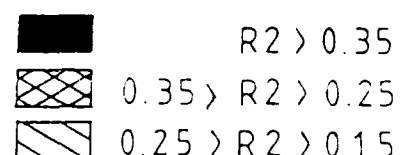
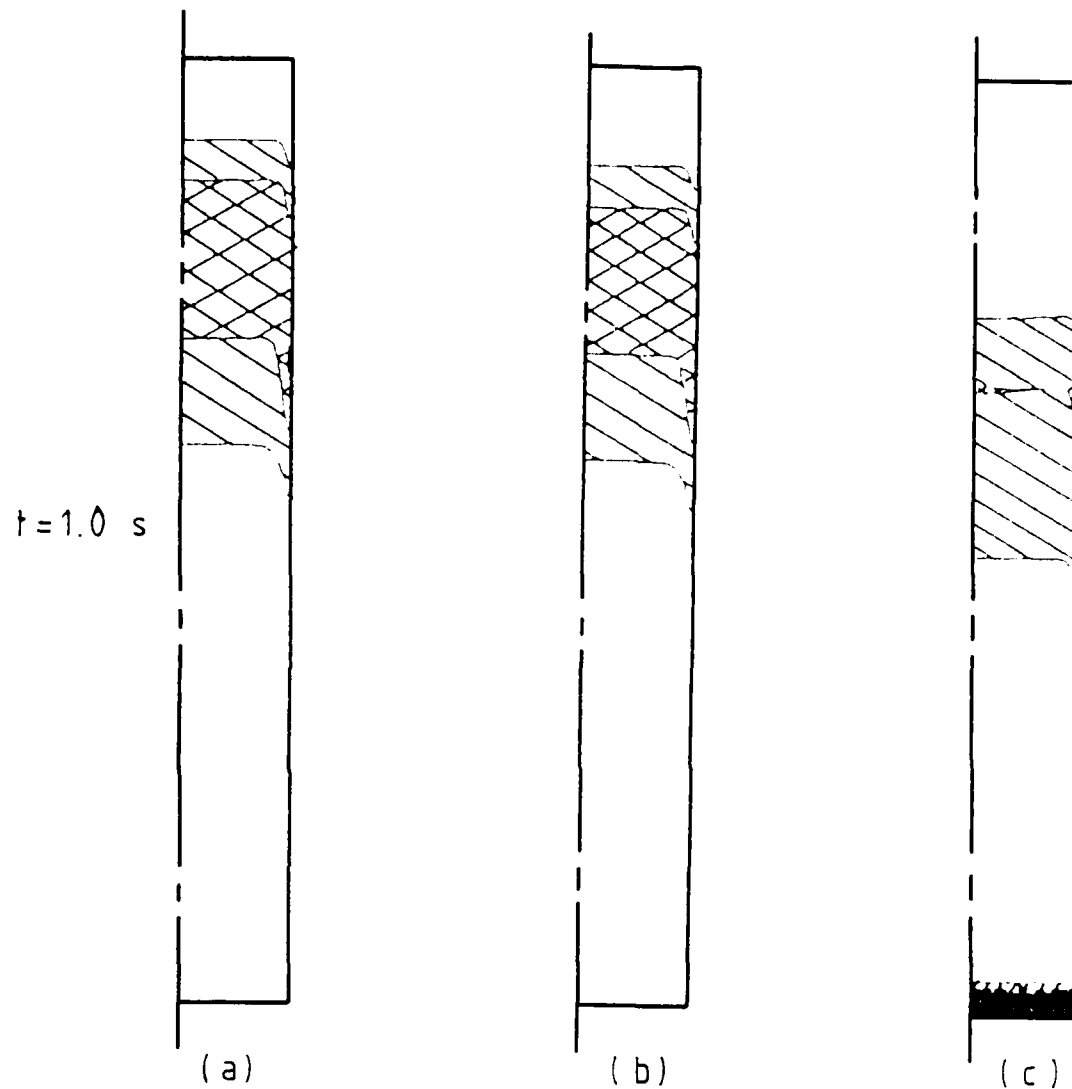


Figure 6 (cont'd) : The effect of CFIPS

(a) CFIPS =  $10^6$   
 (b) CFIPS =  $10^3$   
 (c) CFIPS =  $10^2$

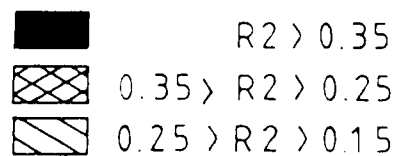
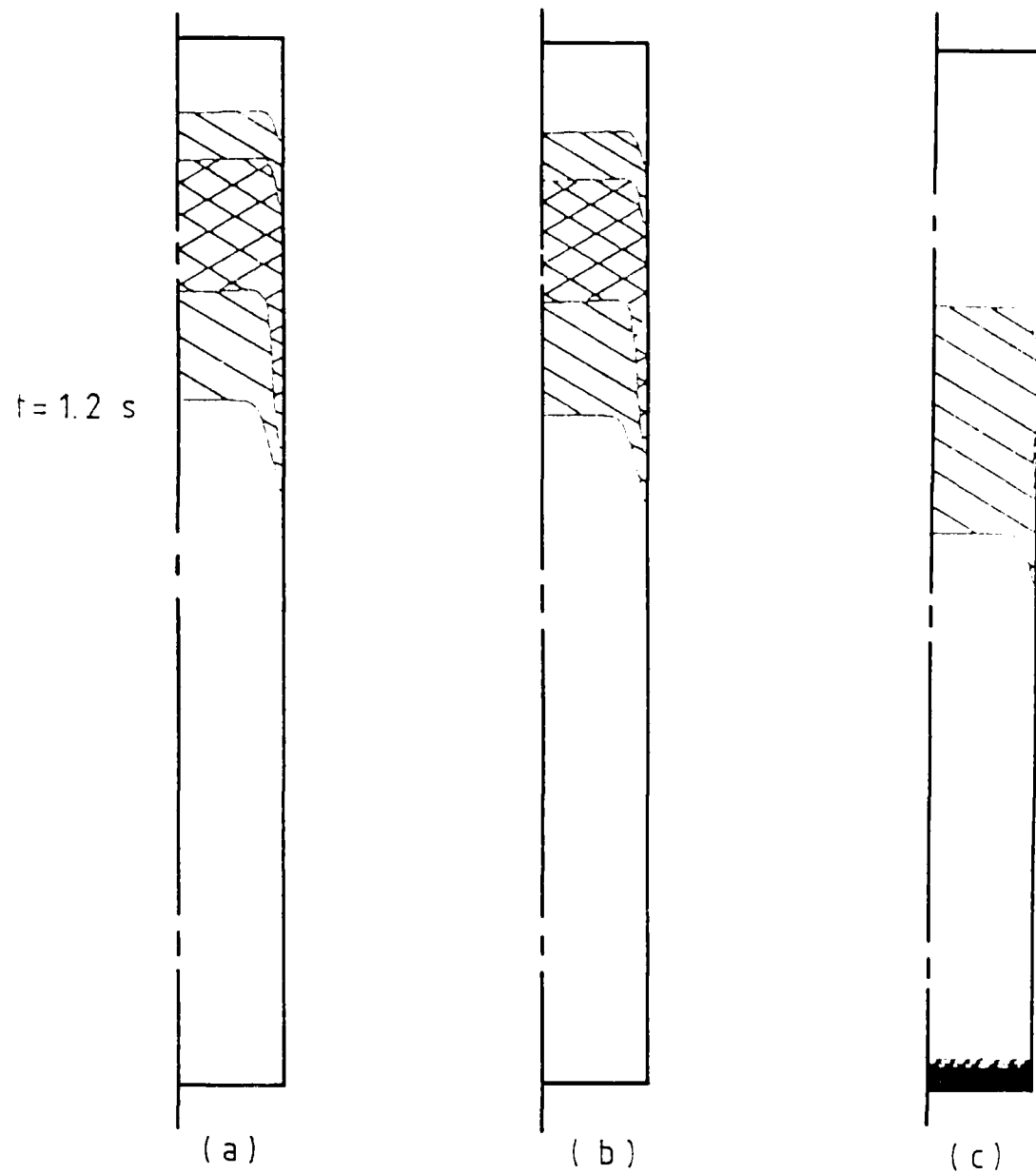


Figure 6 (cont'd) : The effect of CFIPS  
 (a)  $CFPIS = 10^6$   
 (b)  $CFPIS = 10^3$   
 (c)  $CFPIS = 10^2$

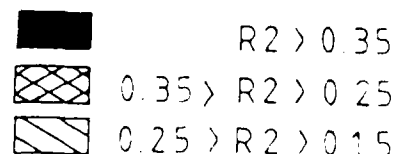
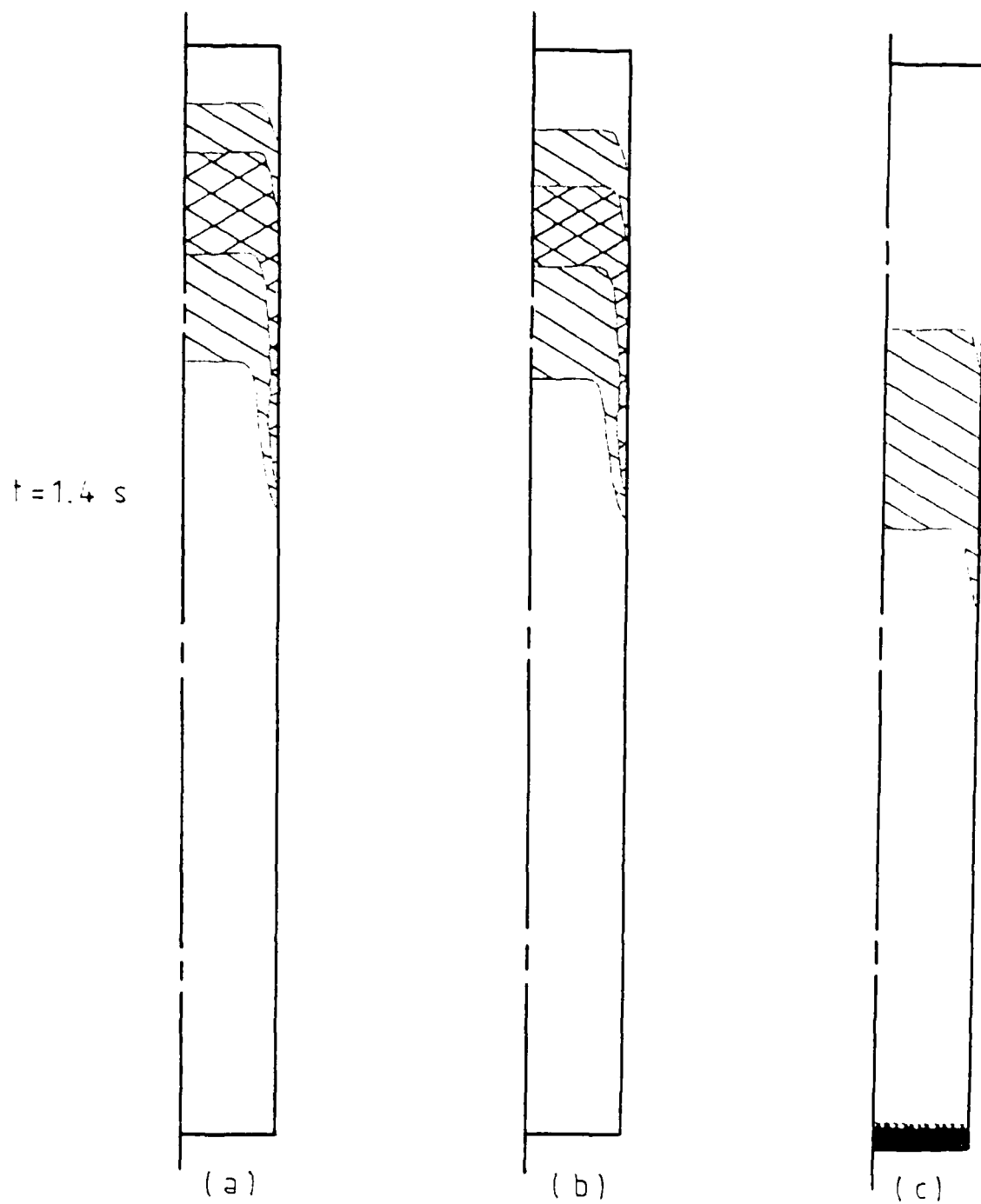


Figure 6 (cont'd) : The effect of CFIPS  
 (a)  $CFPIS = 10^6$   
 (b)  $CFPIS = 10^3$   
 (c)  $CFPIS = 10^2$

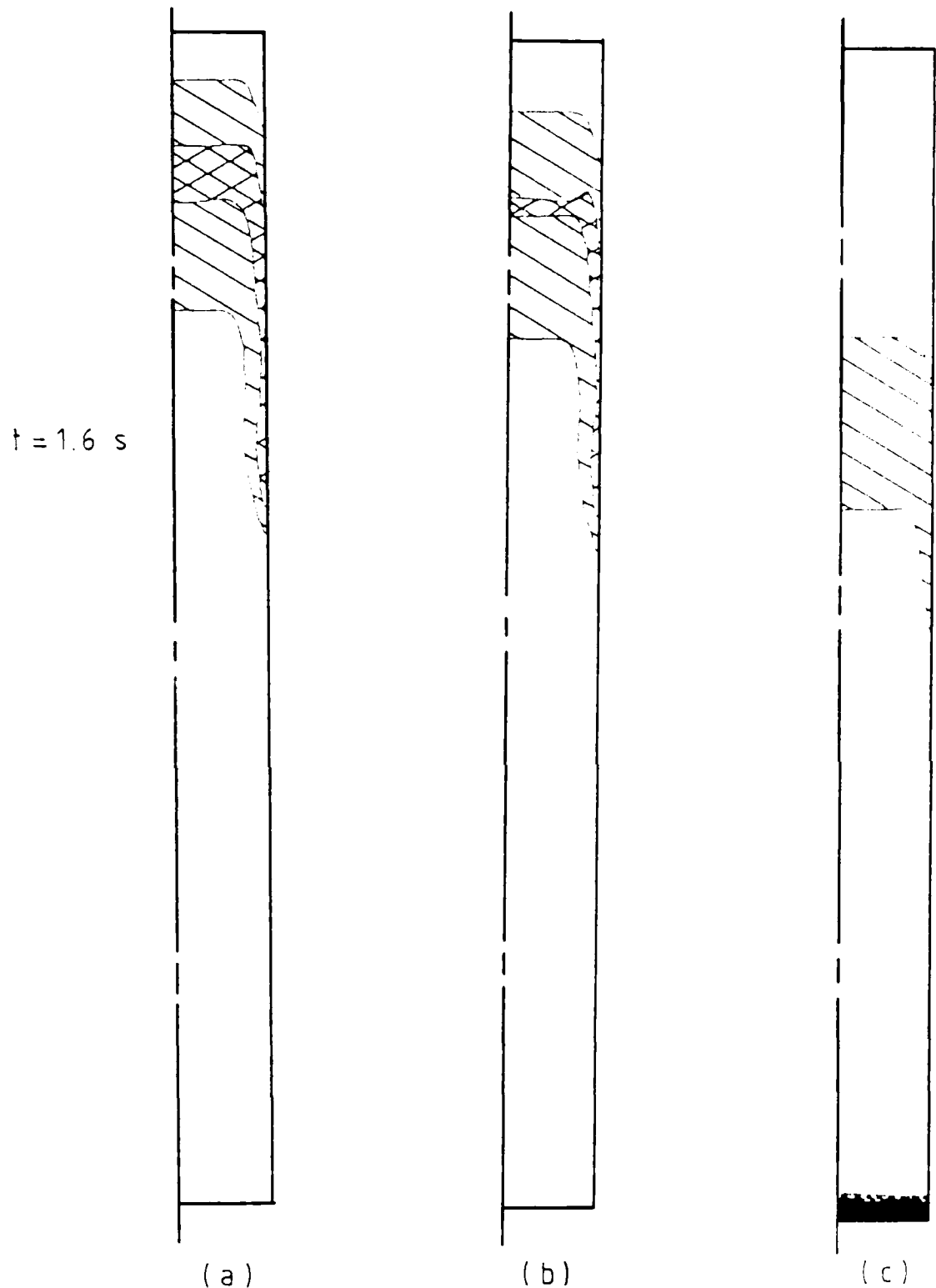
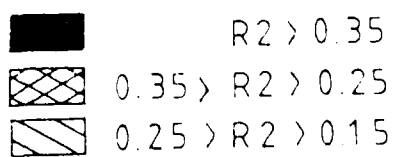


Figure 6 (cont'd) : The effect of CFPIS

The effect of C

- CFPIS =  $10^6$
- CFPIS =  $10^3$
- CFPIS =  $10^2$



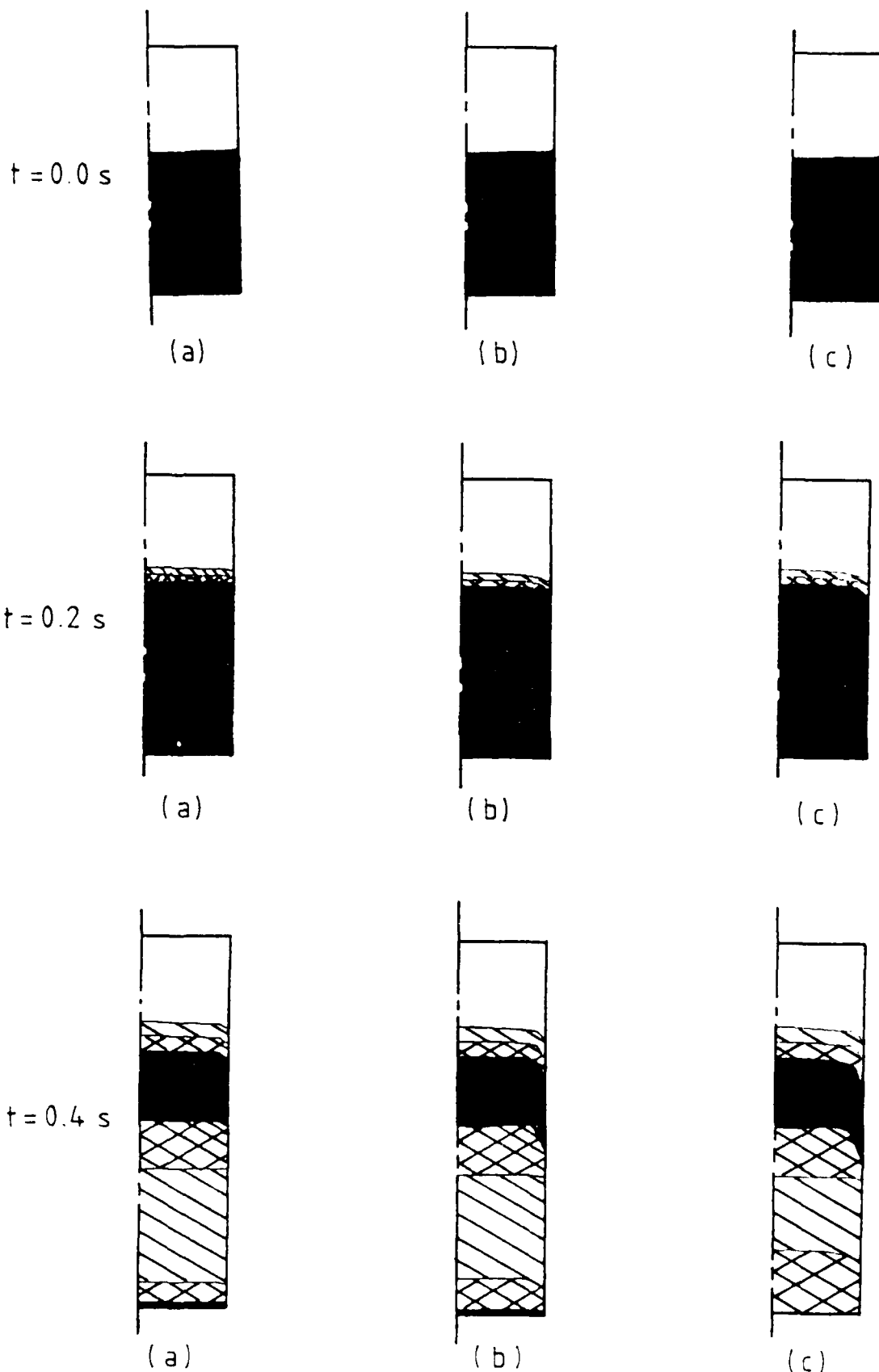


Figure 7 : The effect of viscosity  
 (a)  $k = 3.9$   
 (b)  $k = 10$   
 (c)  $k = 15$

■	$R2 > 0.35$
▨	$0.35 > R2 > 0.25$
▨	$0.25 > R2 > 0.15$

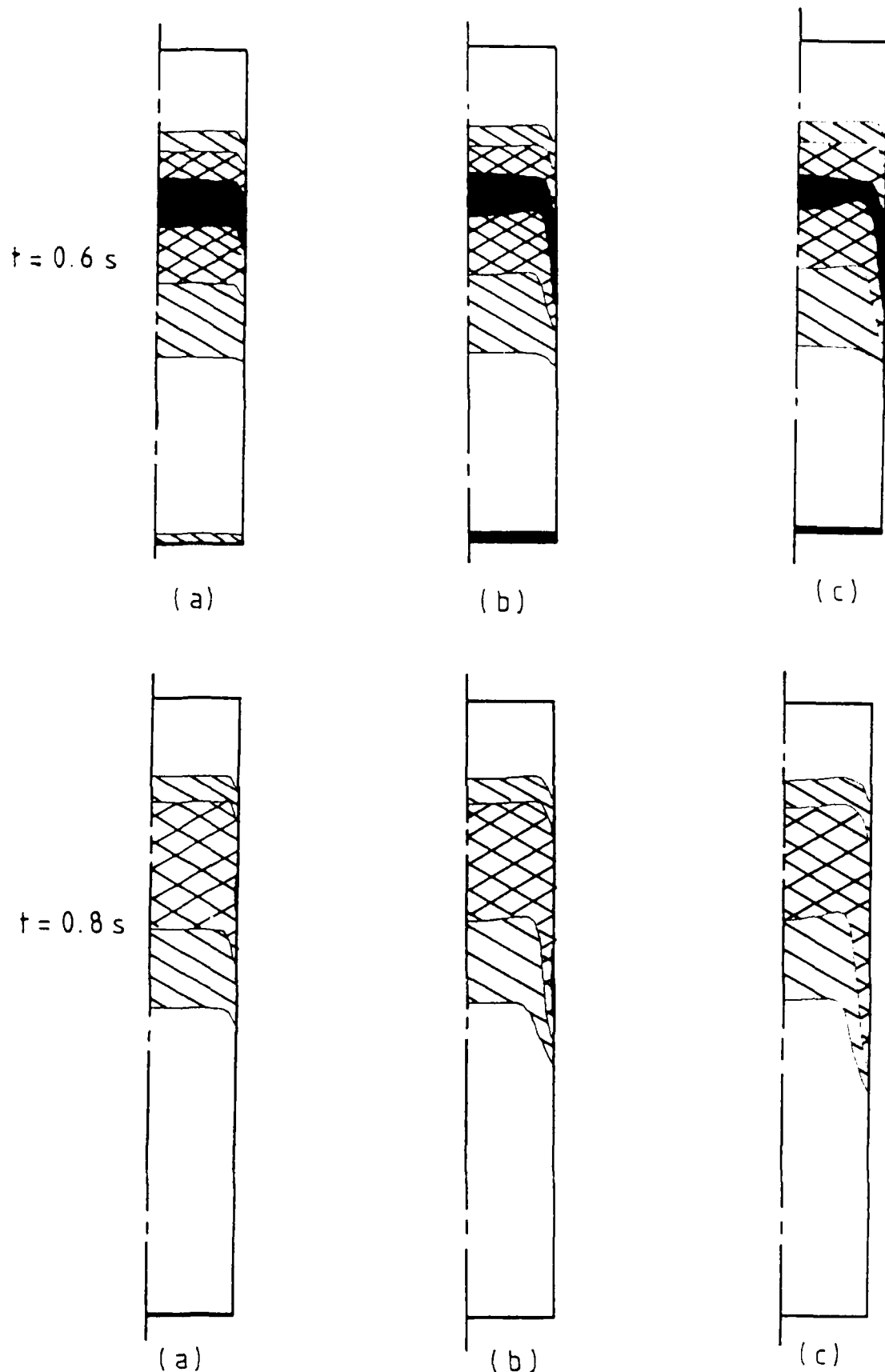


Figure 7 (cont'd) : The effect of viscosity

(a)  $k = 3.9$

(b)  $k = 10$

(c)  $k = 15$



$R2 > 0.35$



$0.35 > R2 > 0.25$



$0.25 > R2 > 0.15$

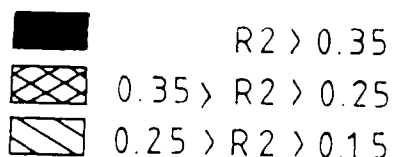
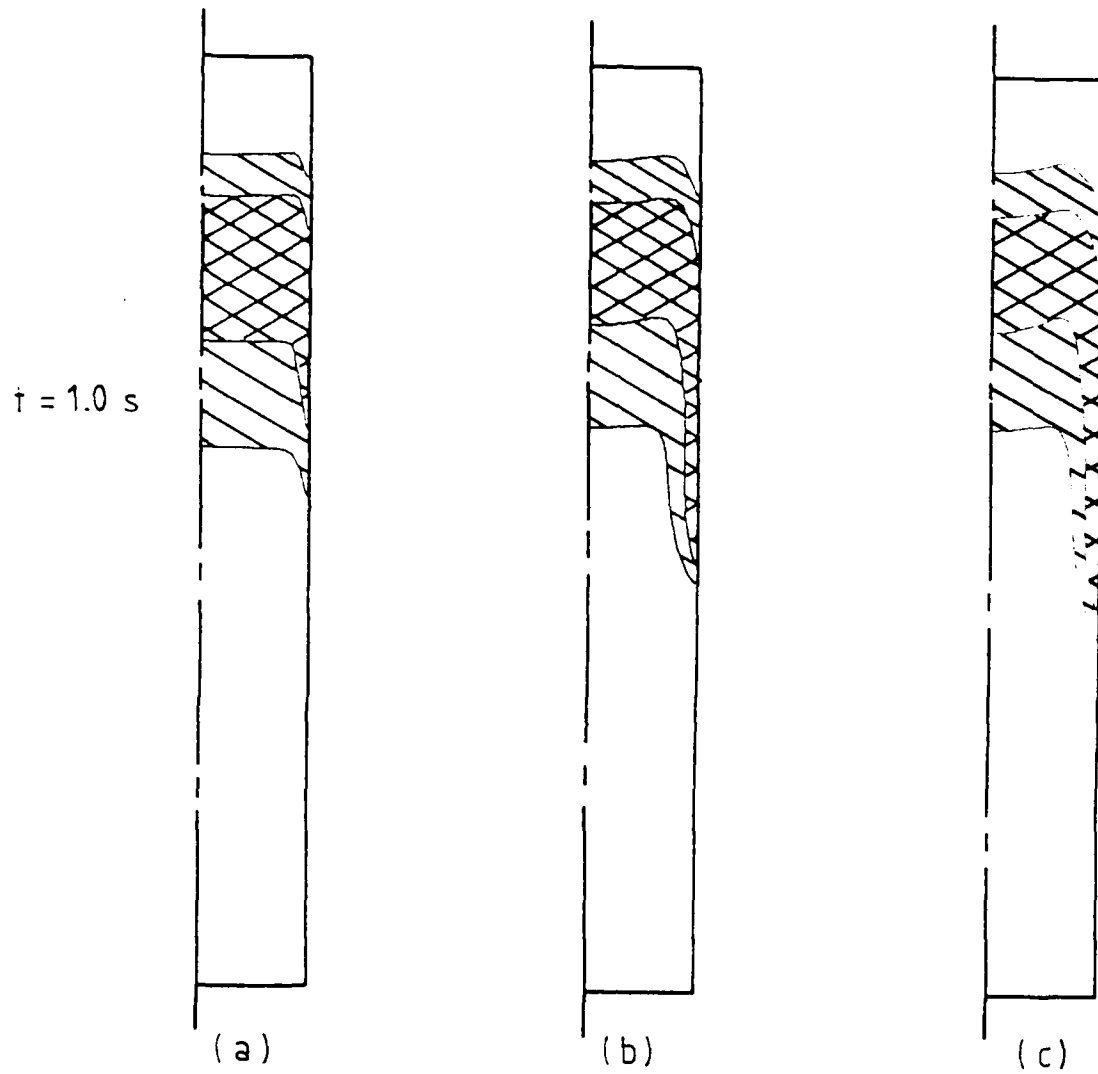


Figure 7 (cont'd) : The effect of viscosity

- (a)  $k = 3.9$
- (b)  $k = 10$
- (c)  $k = 15$

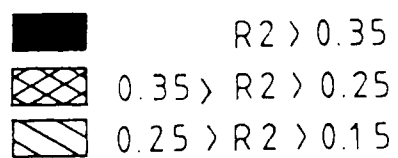
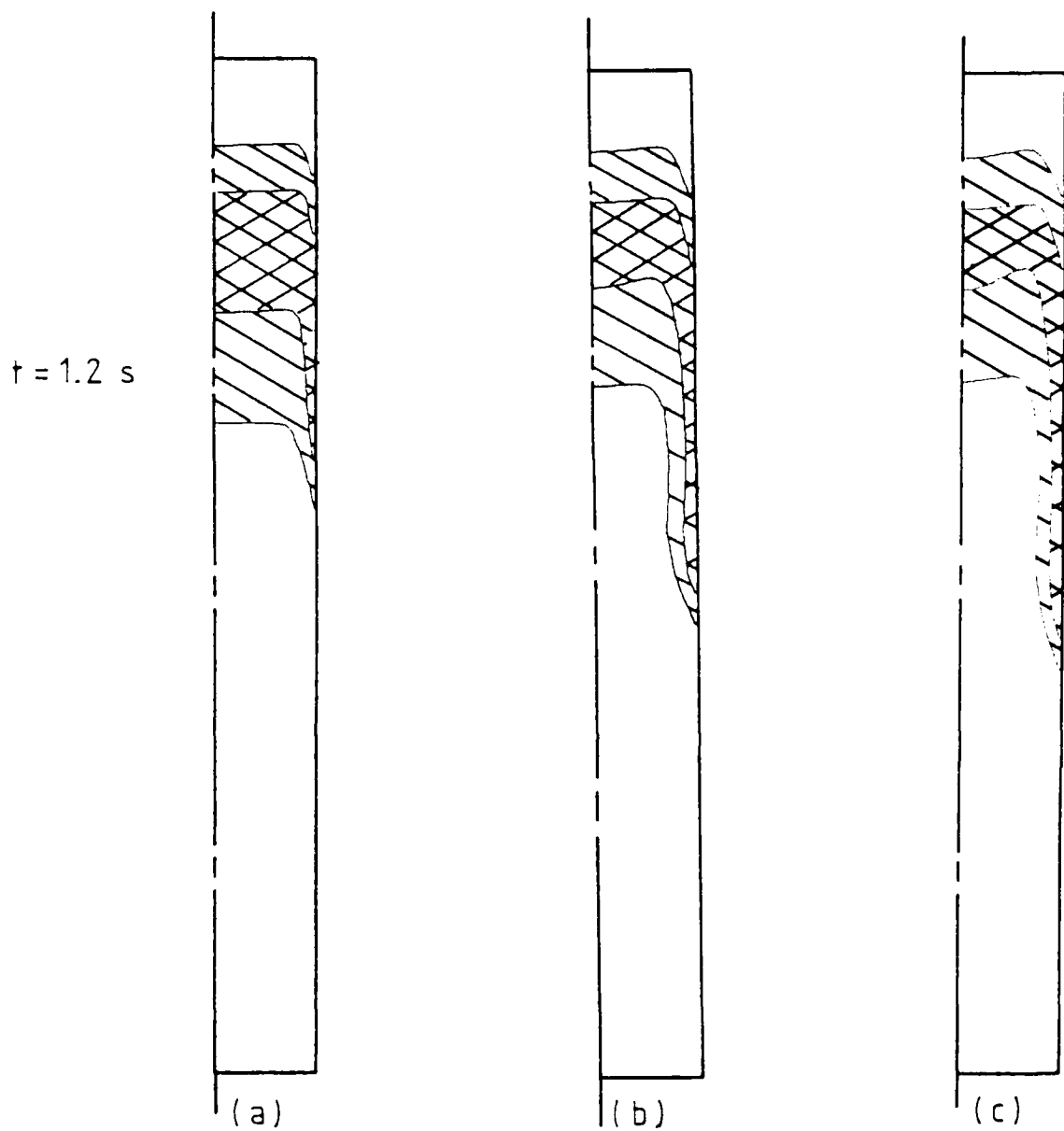


Figure 7 (cont'd) : The effect of viscosity

- (a)  $k = 3.9$
- (b)  $k = 10$
- (c)  $k = 15$

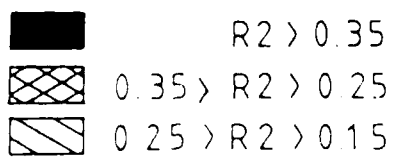
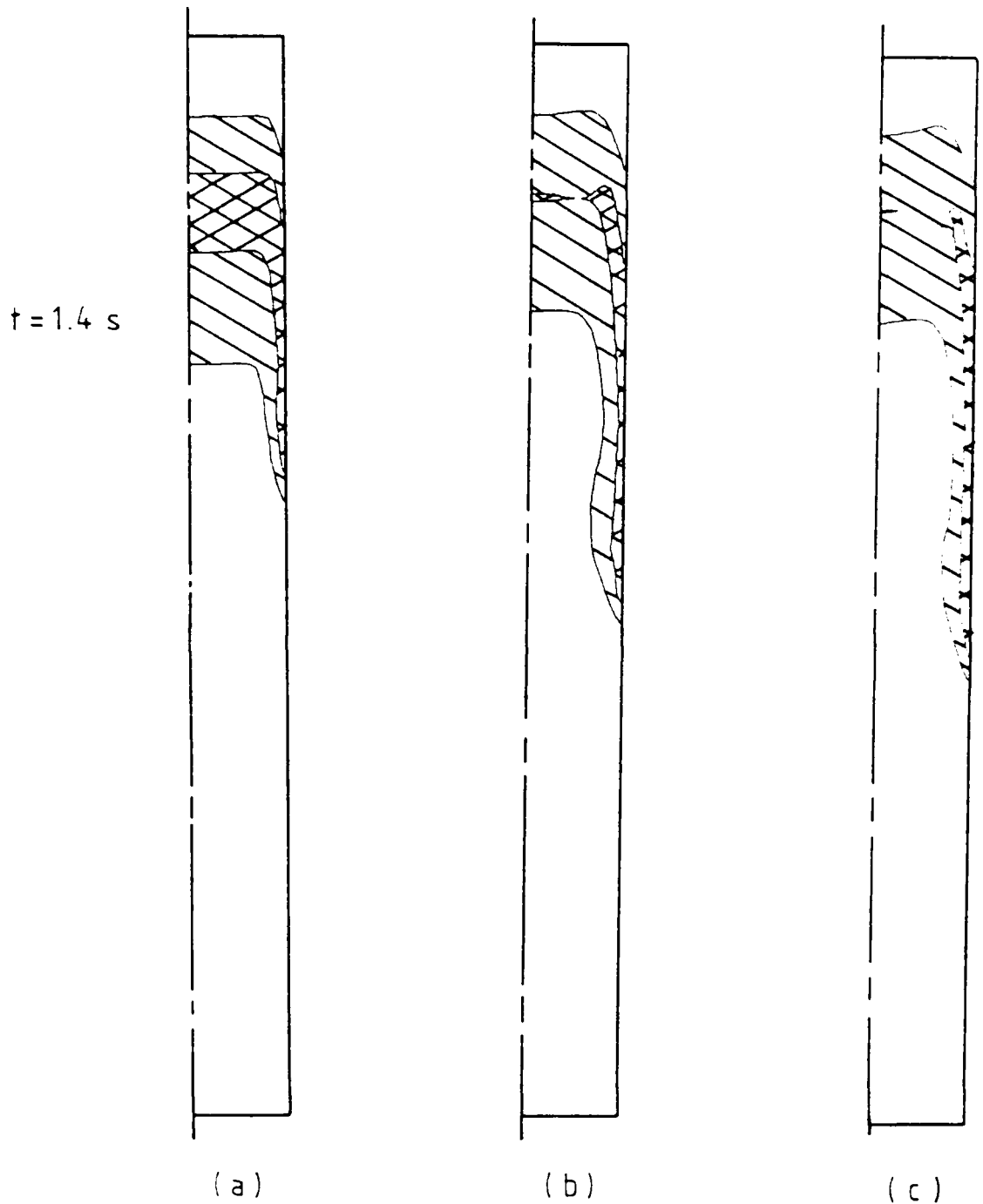


Figure 7 (cont'd) : The effect of viscosity

- (a)  $k = 3.9$
- (b)  $k = 10$
- (c)  $k = 15$

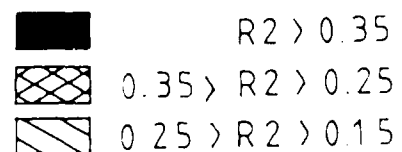
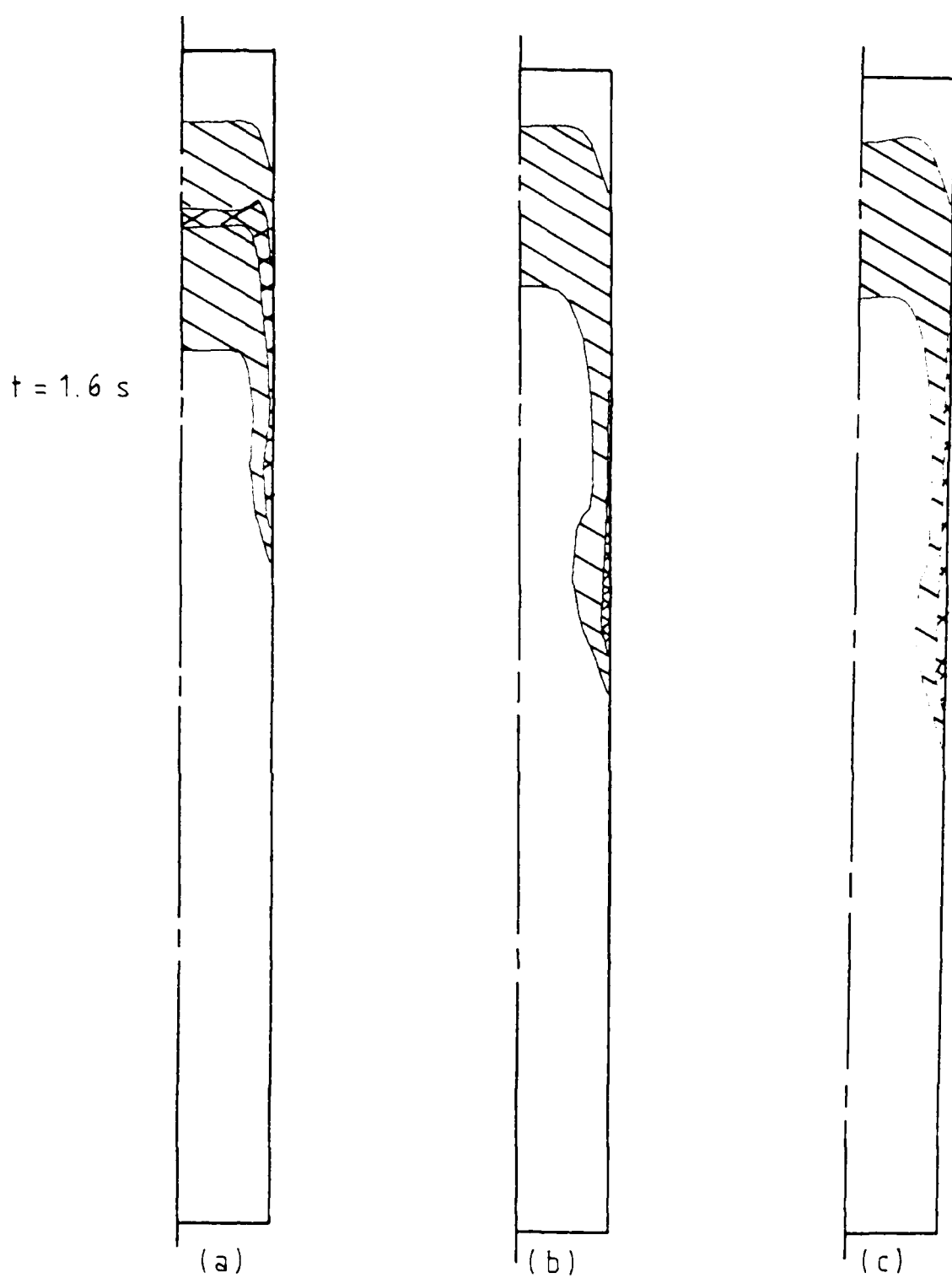


Figure 7 (cont'd) : The effect of viscosity

- (a)  $k = 3.9$
- (b)  $k = 10$
- (c)  $k = 15$

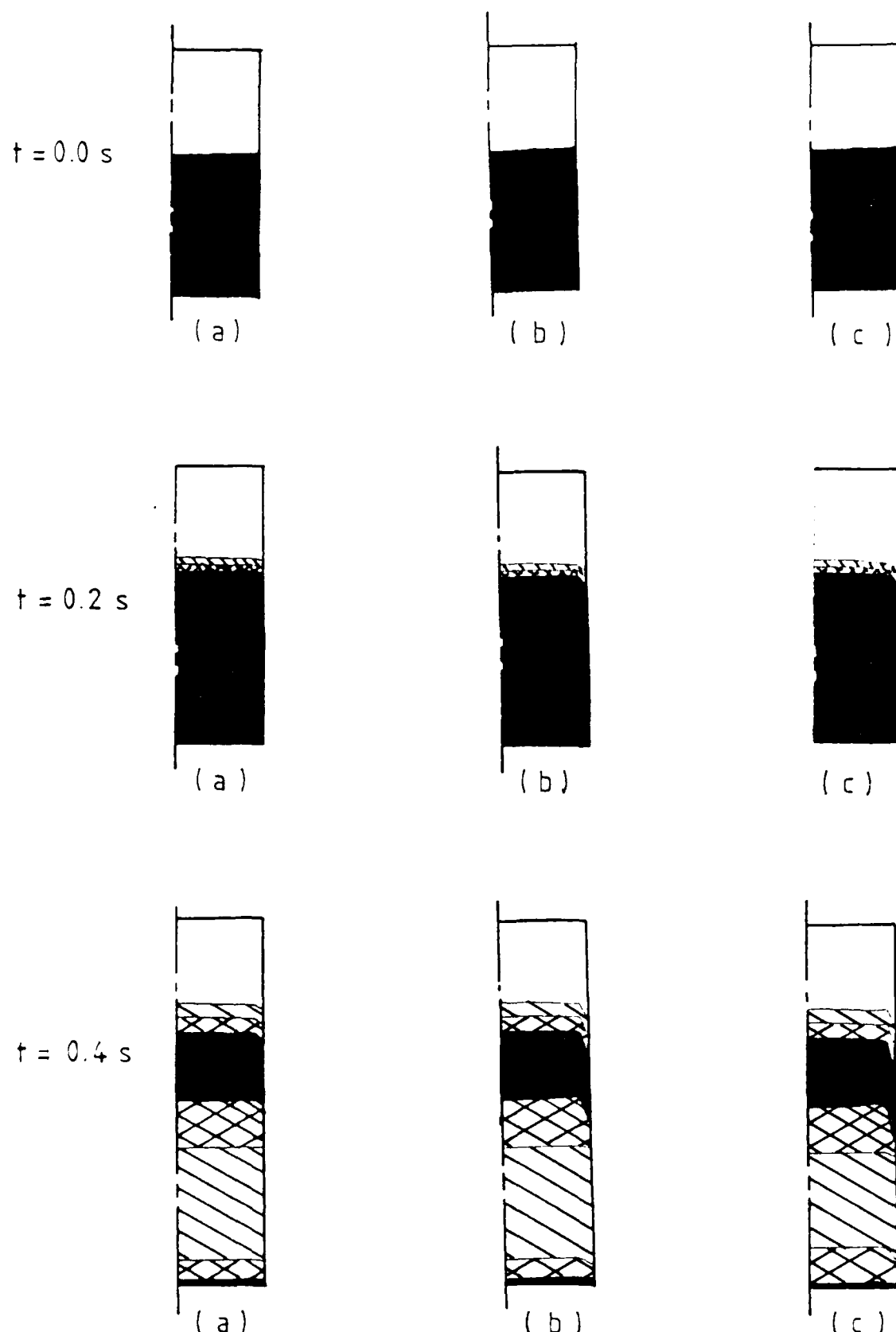


Figure 8 : The effect of the wall

- (a)  $c = 1 \text{ & } k = 3.9$
- (b)  $c = 10 \text{ & } k = 3.9$
- (c)  $c = 10 \text{ & } k = 10$

$R2 > 0.35$	
$0.35 > R2 > 0.25$	
$0.25 > R2 > 0.15$	

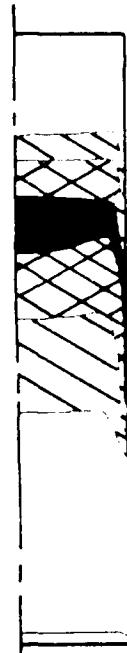
$t = 0.6 \text{ s}$



(a)



(b)



(c)

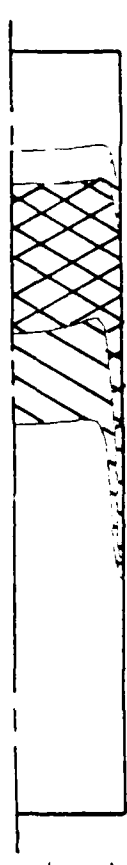
$t = 0.8 \text{ s}$



(a)



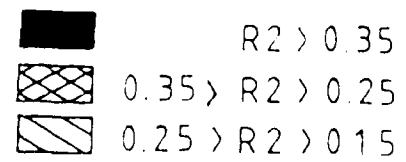
(b)



(c)

Figure 8 (cont'd) : The effect of the wall

- (a)  $c = 1 \text{ & } k = 3.9$
- (b)  $c = 10 \text{ & } k = 3.9$
- (c)  $c = 10 \text{ & } k = 10$



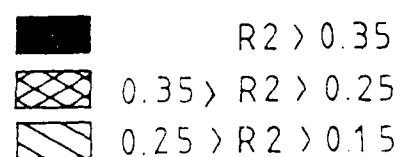
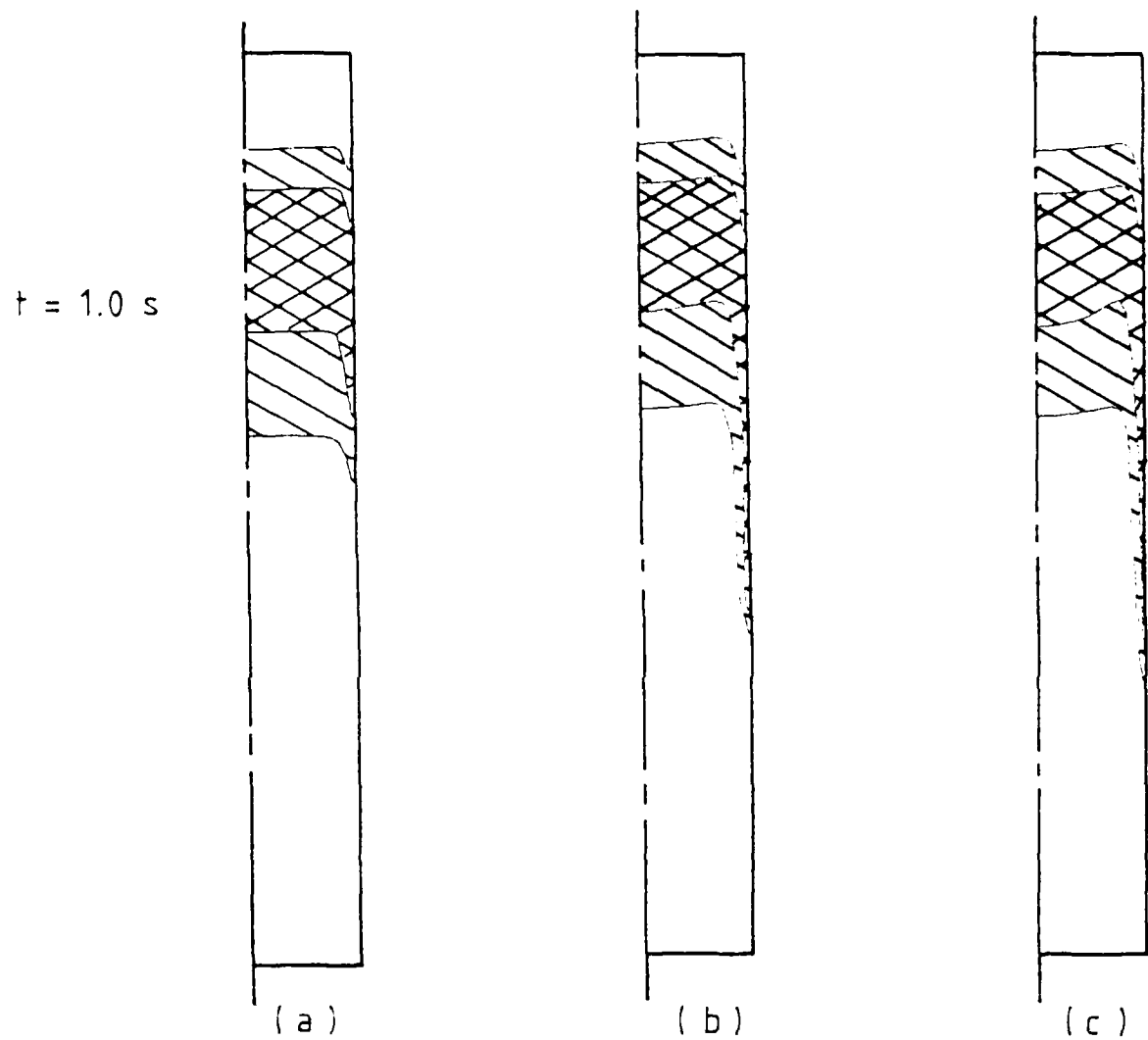


Figure 8 (cont'd) : The effect of the wall

- (a)  $c = 1 \text{ & } k = 3.9$
- (b)  $c = 10 \text{ & } k = 3.9$
- (c)  $c = 10 \text{ & } k = 10$

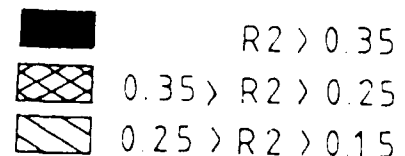
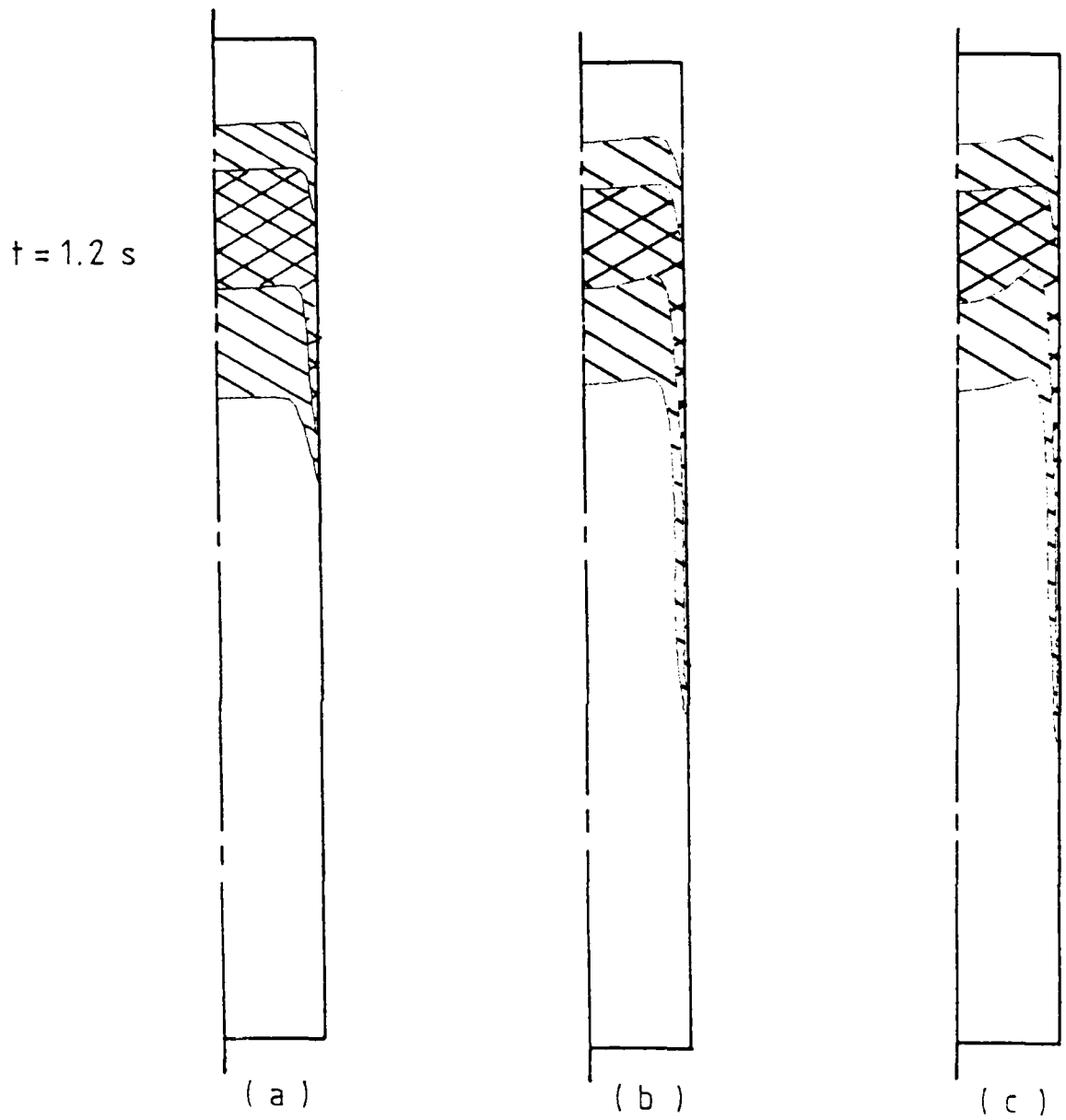


Figure 8 (cont'd) : The effect of the wall

(a)  $c = 1$  &  $k = 3.9$   
 (b)  $c = 10$  &  $k = 3.9$   
 (c)  $c = 10$  &  $k = 10$

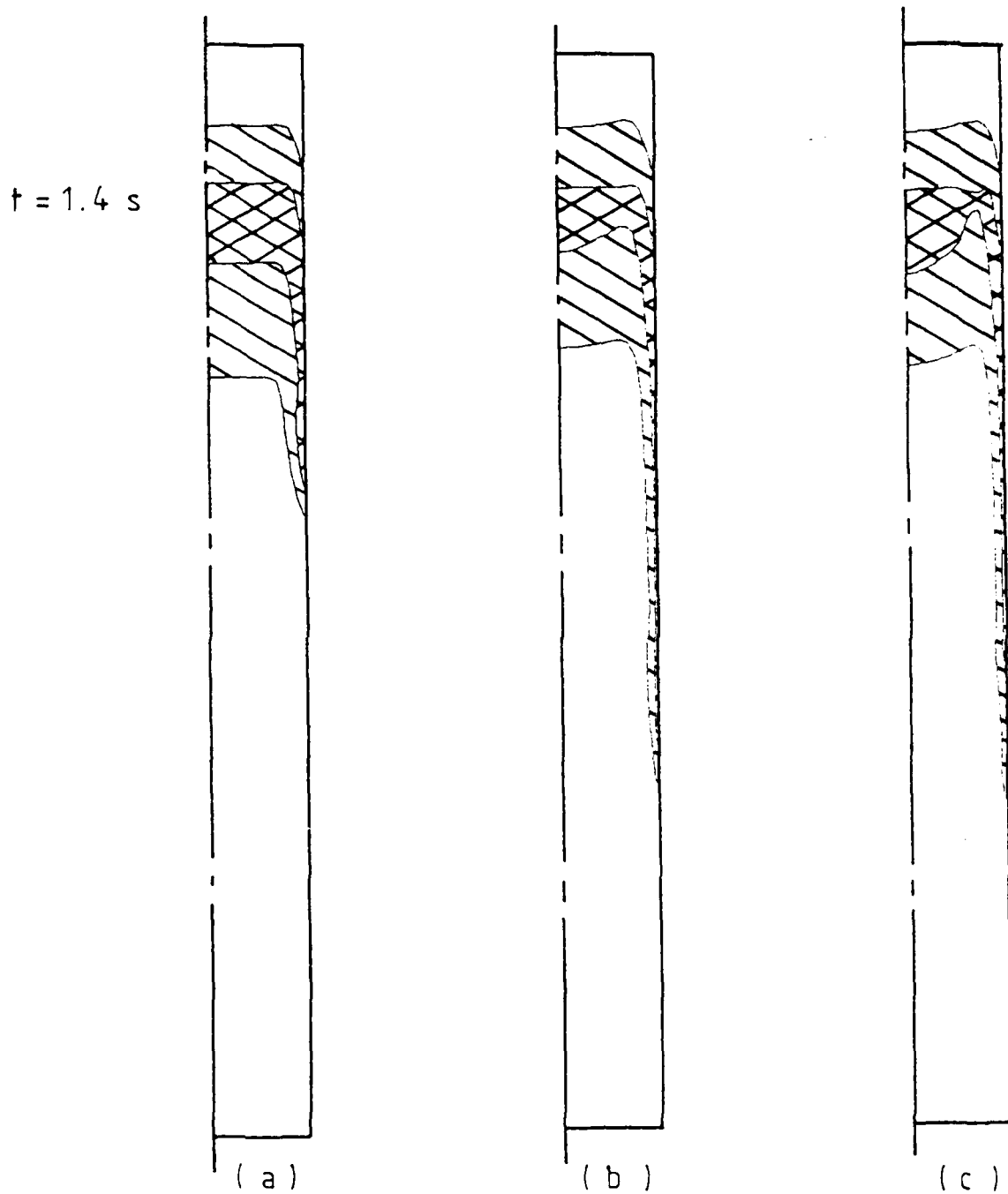


Figure 8 (cont'd) : The effect of the wall  
 (a)  $c = 1$  &  $k = 3.9$   
 (b)  $c = 10$  &  $k = 3.9$   
 (c)  $c = 10$  &  $k = 10$

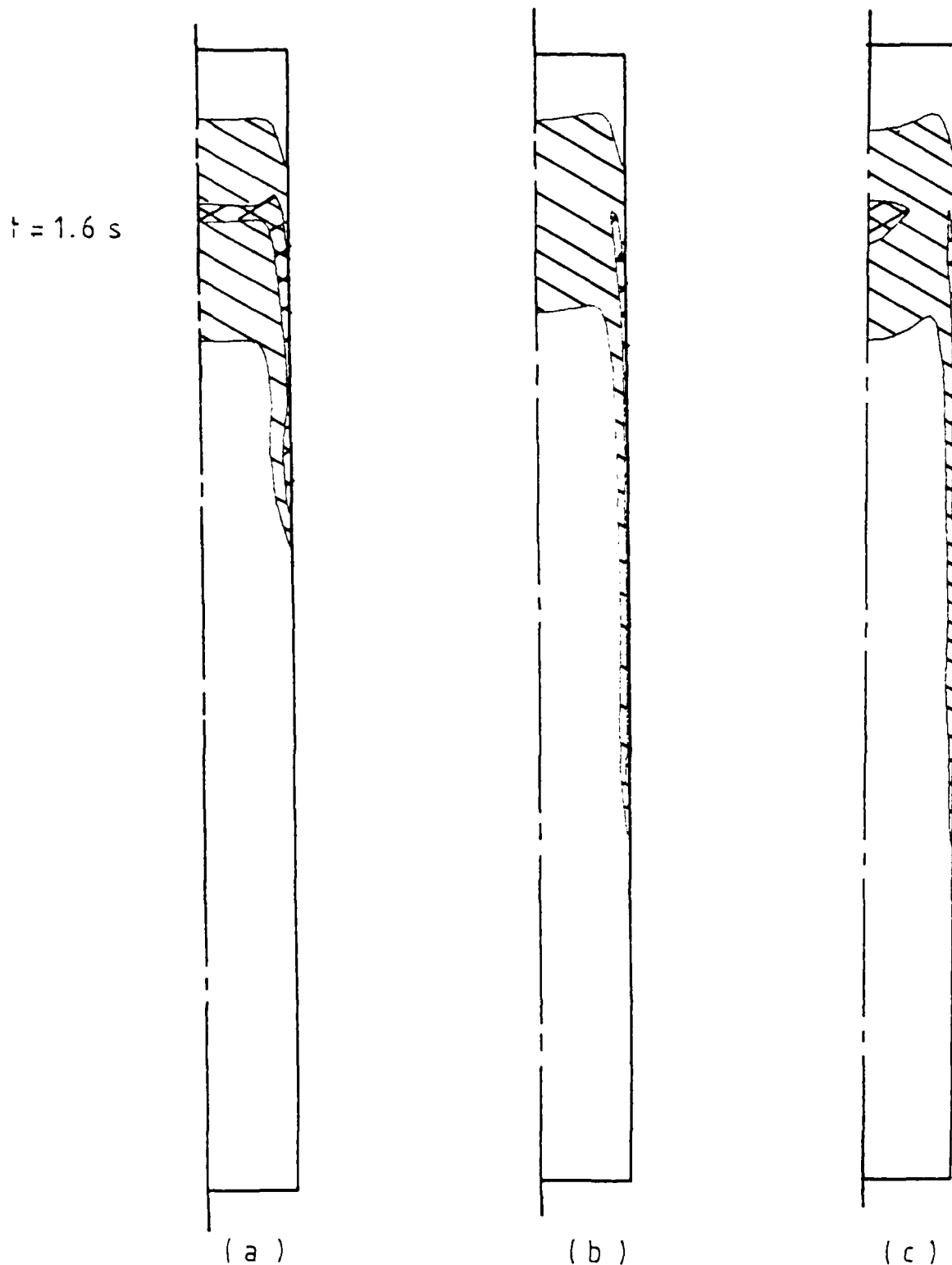


Figure 8 (cont'd) : The effect of the wall

(a)  $c = 1$  &  $k = 3.9$   
 (b)  $c = 10$  &  $k = 3.9$   
 (c)  $c = 10$  &  $k = 10$



R<sup>2</sup> > 0.35



$$0.35 > R^2 > 0.25$$



$$0.25 > R^2 > 0.15$$



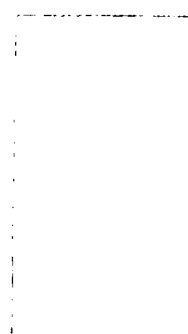
$t = 0.0 \text{ s}$



R2 CONTOUR PLOT



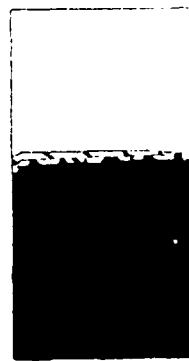
H1 VECTOR PLOT



H2 VECTOR PLOT



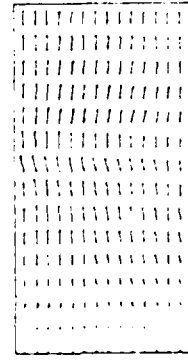
$t = 0.2 \text{ s}$



R2 CONTOUR PLOT



H1 VECTOR PLOT



H2 VECTOR PLOT



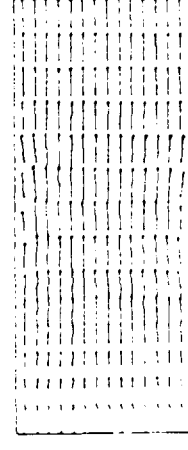
$t = 0.4 \text{ s}$



R2 CONTOUR PLOT

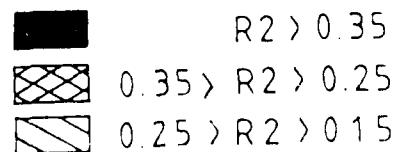


H1 VECTOR PLOT



H2 VECTOR PLOT

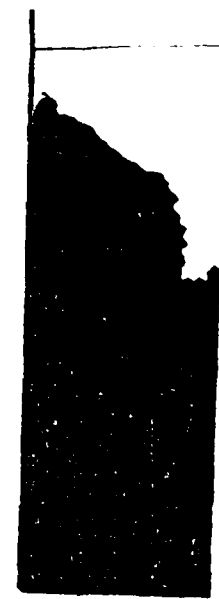
Figure 9 : Prediction of the experiment with a tilted interface



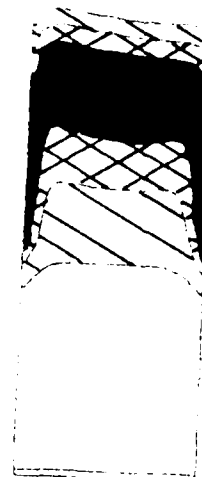
$R2 > 0.35$

$0.35 > R2 > 0.25$

$0.25 > R2 > 0.15$



$t = 0.6 \text{ s}$



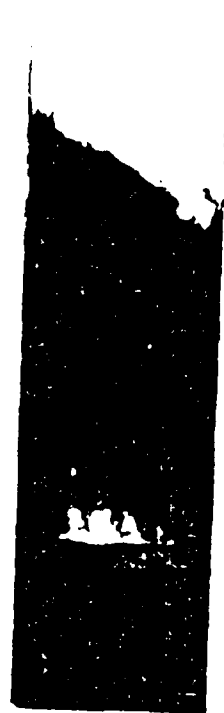
R2 CONTOUR PLOT



W1 VECTOR PLOT



W2 VECTOR PLOT



$t = 0.8 \text{ s}$



R2 CONTOUR PLOT



W1 VECTOR PLOT



W2 VECTOR PLOT

Figure 9 (cont'd) : Prediction of the experiment with a tilted interface



$R2 > 0.35$



$0.35 > R2 > 0.25$



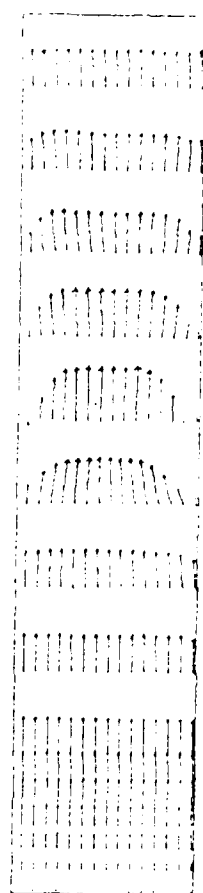
$0.25 > R2 > 0.15$



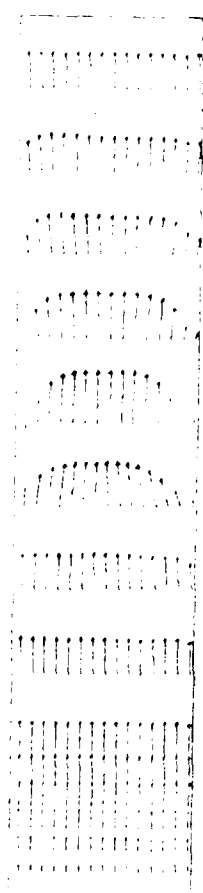
$t = 1.0 \text{ s}$



R2 CONTOUR PLOT



H1 VECTOR PLOT



H2 VECTOR PLOT

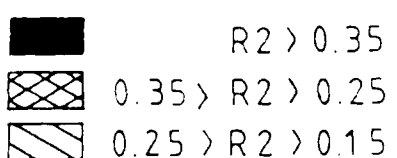


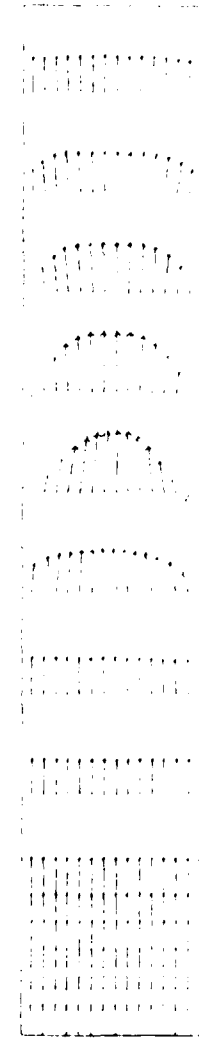
Figure 9 (cont'd) : Prediction of the experiment  
with a tilted interface



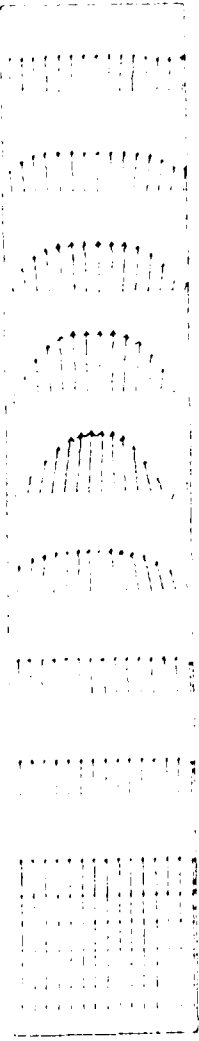
$t = 1.2 \text{ s}$



R2 CONTOUR PLOT



H1 VECTOR PLOT



H2 VECTOR PLOT

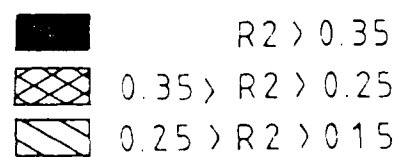
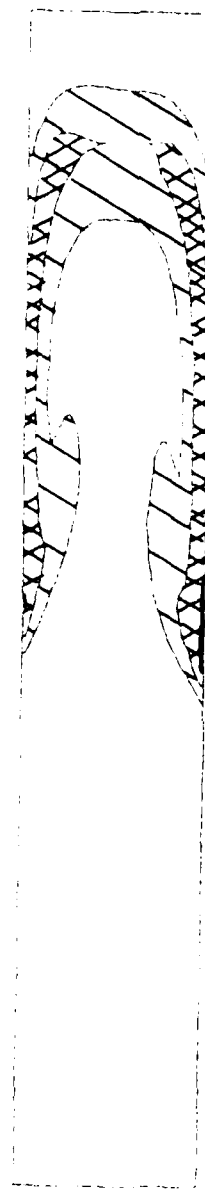


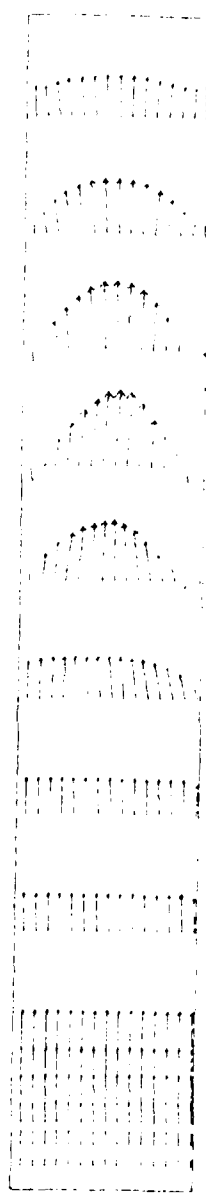
Figure 9 (cont'd) : Prediction of the experiment  
with a tilted interface



$t = 1.4$  s



R2 CONTOUR PLOT



W1 VECTOR PLOT



W2 VECTOR PLOT

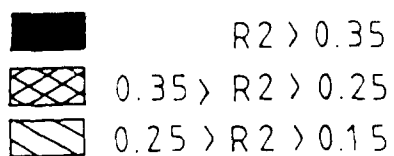
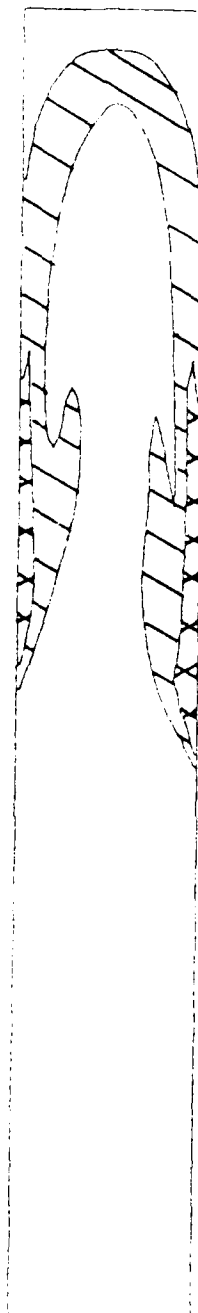


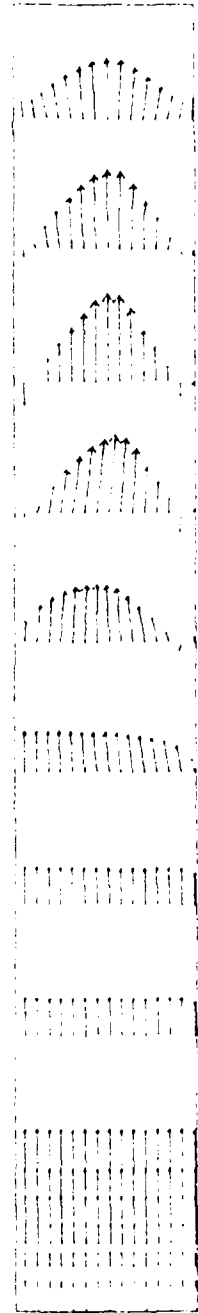
Figure 9 (cont'd) : Prediction of the experiment  
with a tilted interface



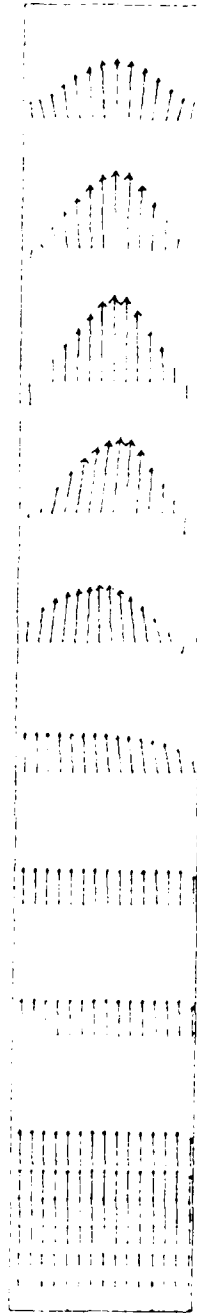
$t = 1.6$  s



R2 CONTOUR PLOT



M1 VECTOR PLOT



M2 VECTOR PLOT

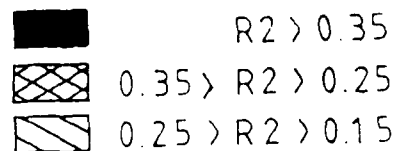


Figure 9 (cont'd) : Prediction of the experiment  
with a tilted interface

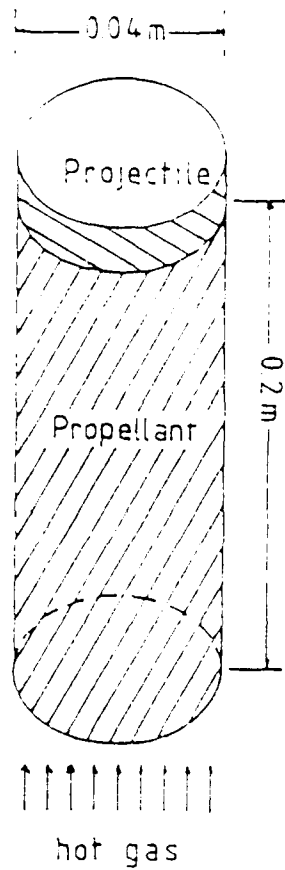


Figure 10:

The gun barrel considered

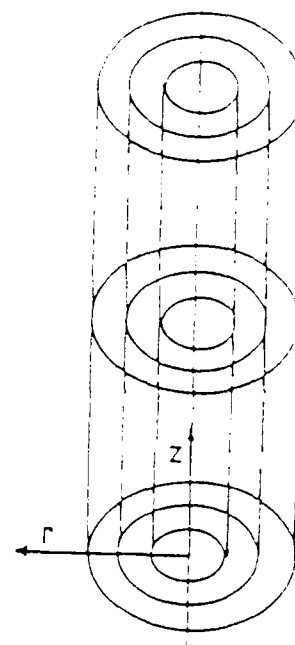
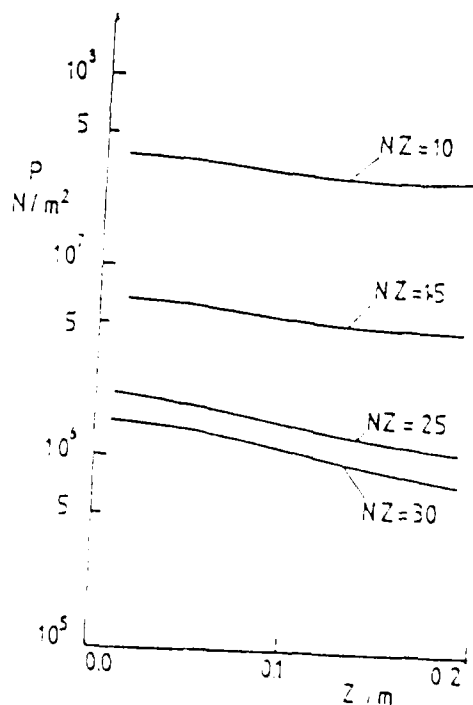


Figure 11

The finite domain grid used

Figure 12

The effect on the pressure of the number of cells used in the axial direction



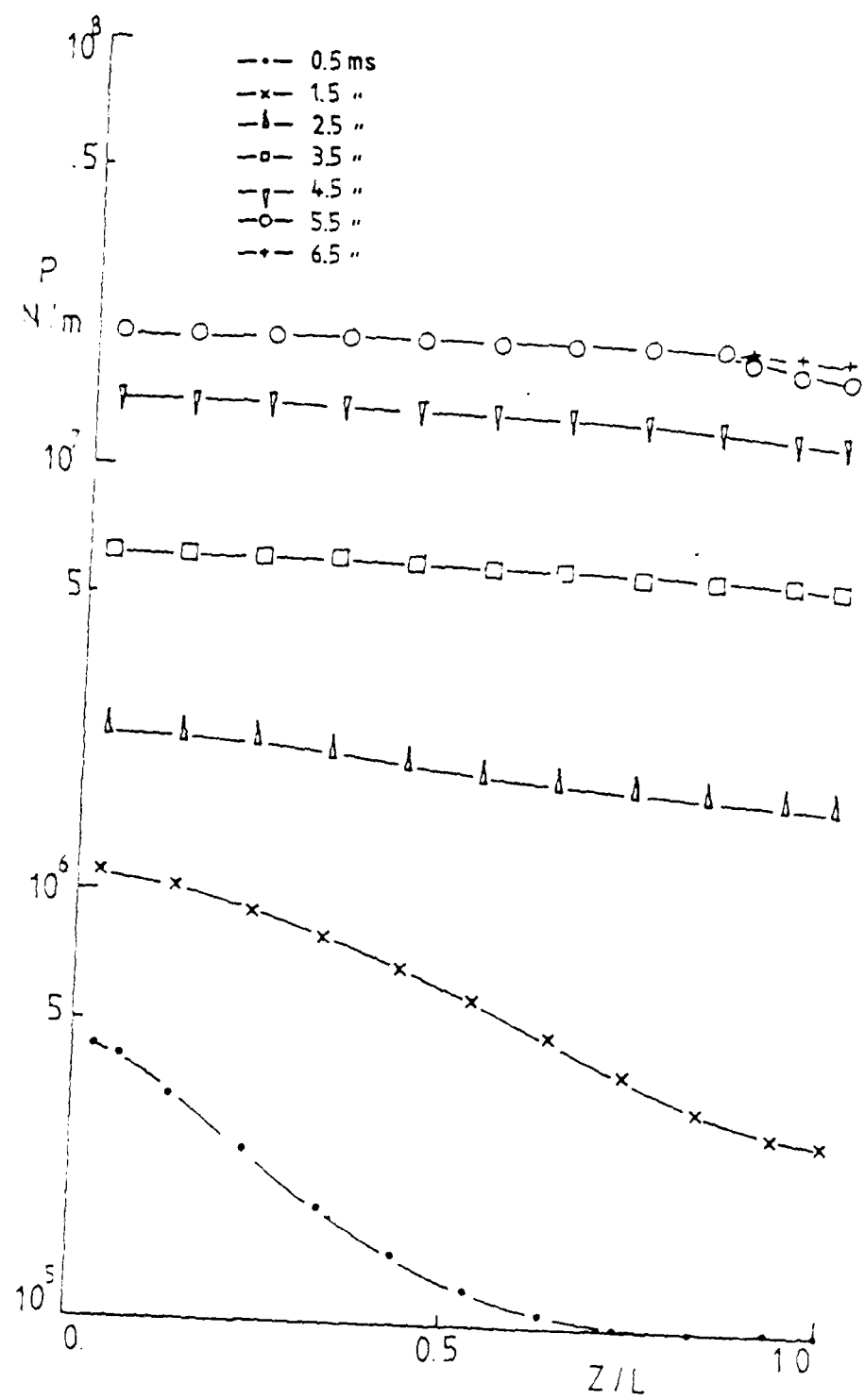


Figure 13

The pressure axial distribution history

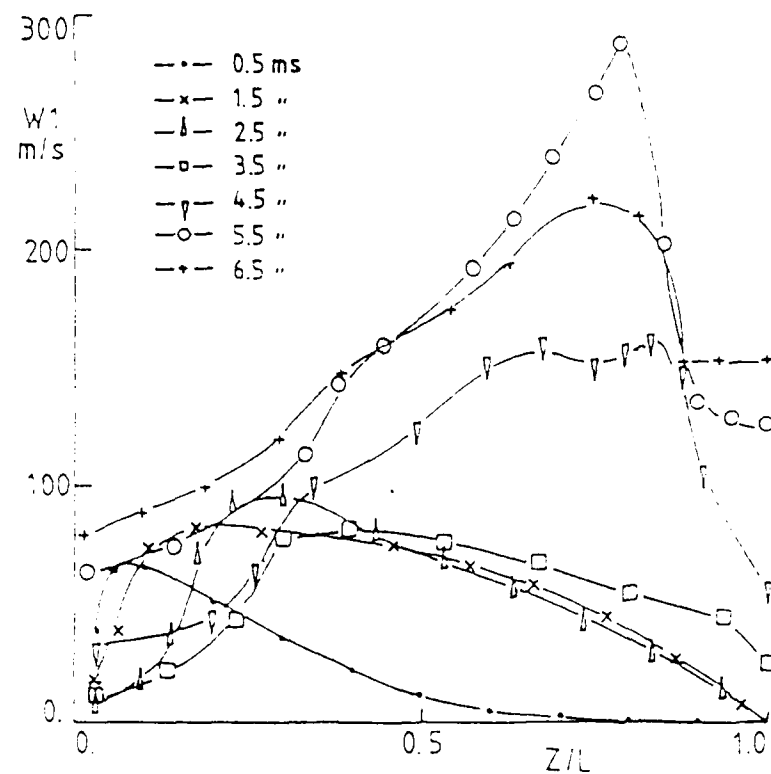


Figure 14

The gas velocity axial distribution history

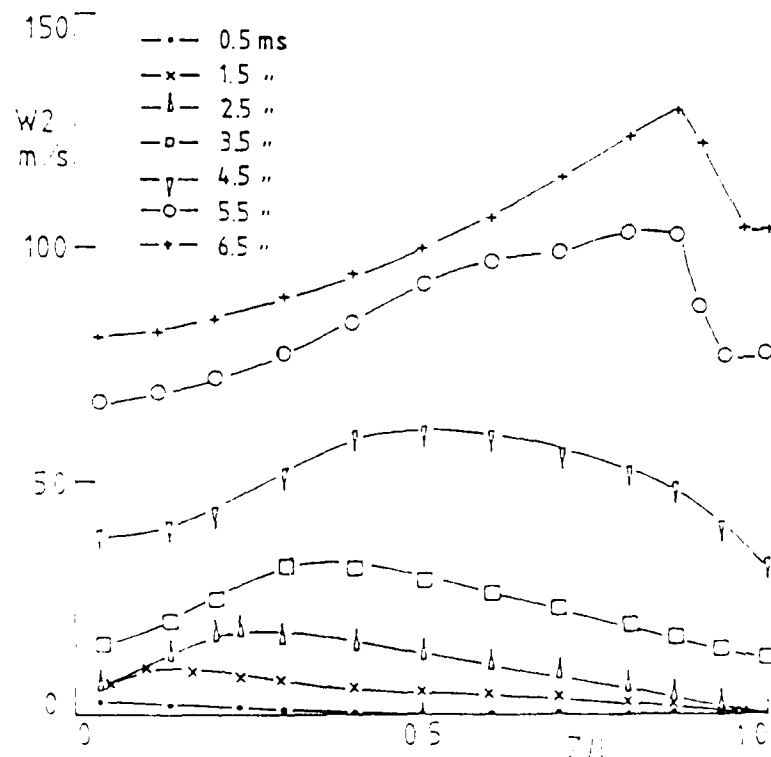


Figure 15

The particle velocity axial distribution history

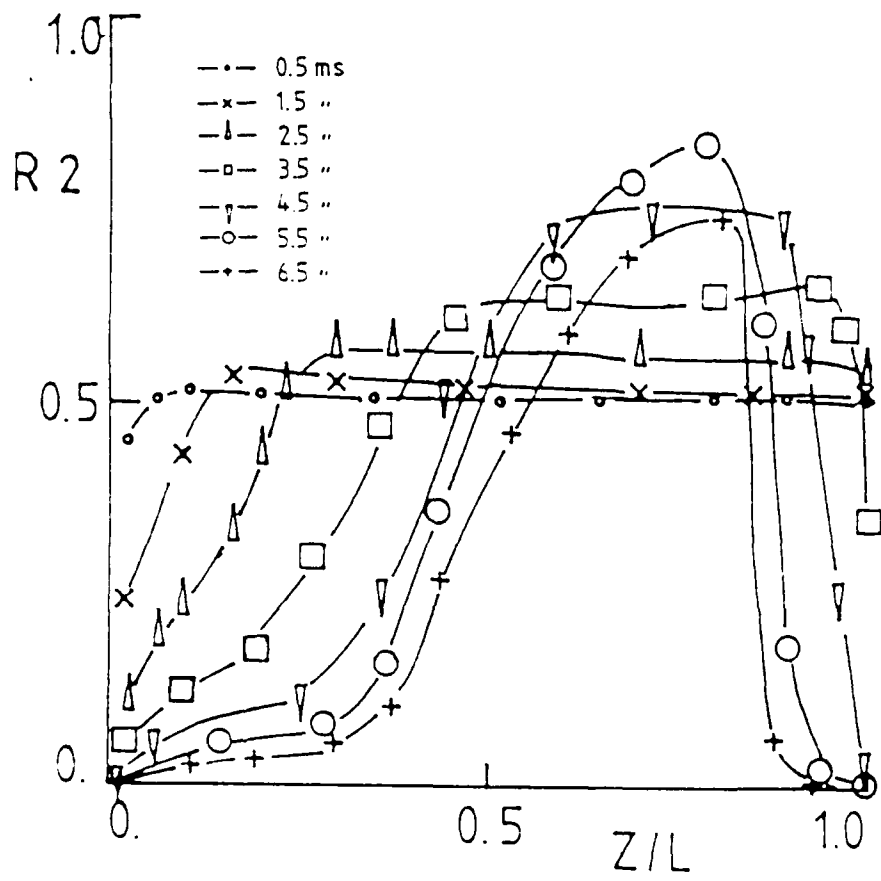


Figure 16

The particle volume fraction axial distribution history

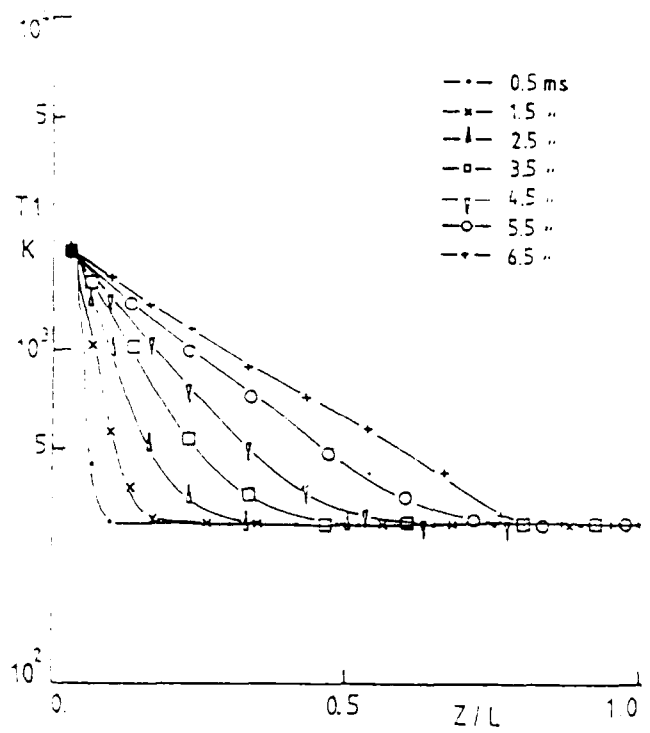


Figure 17

The gas temperature axial distribution history

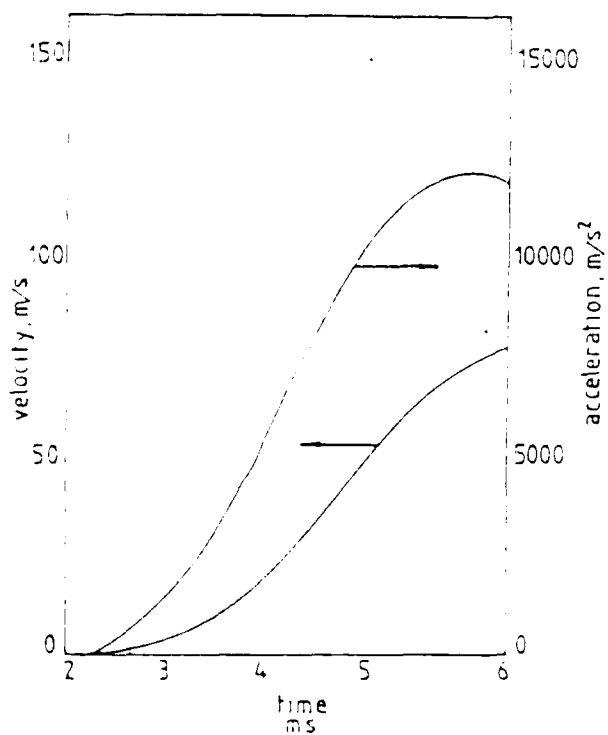


Figure 18

Projectile acceleration and velocity

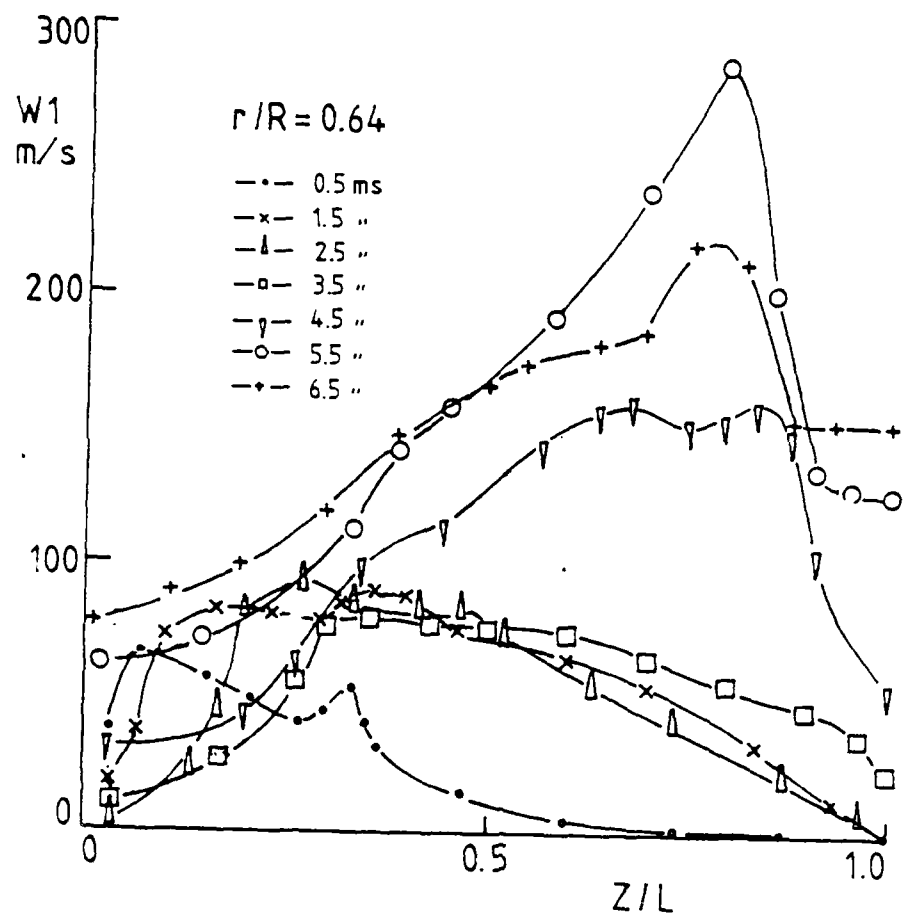


Figure 19

The gas velocity axial distribution history  
at  $r/R = 0.64$

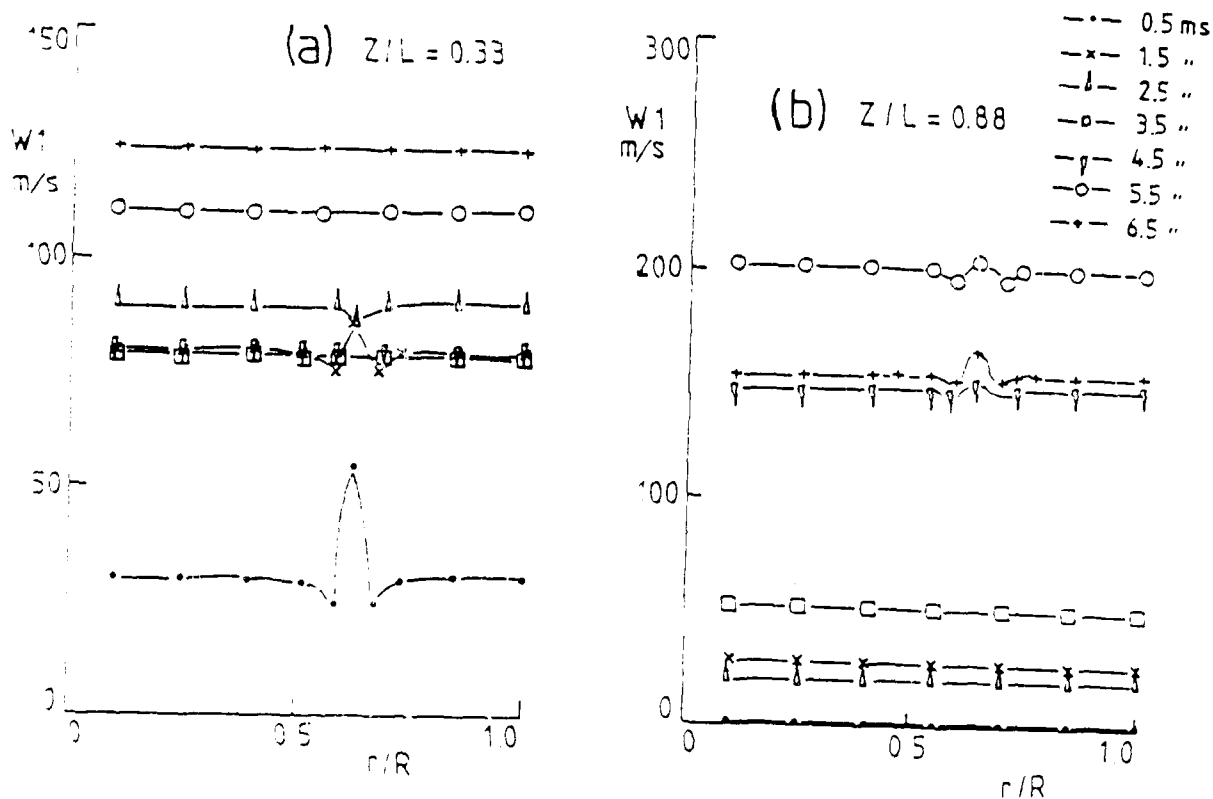
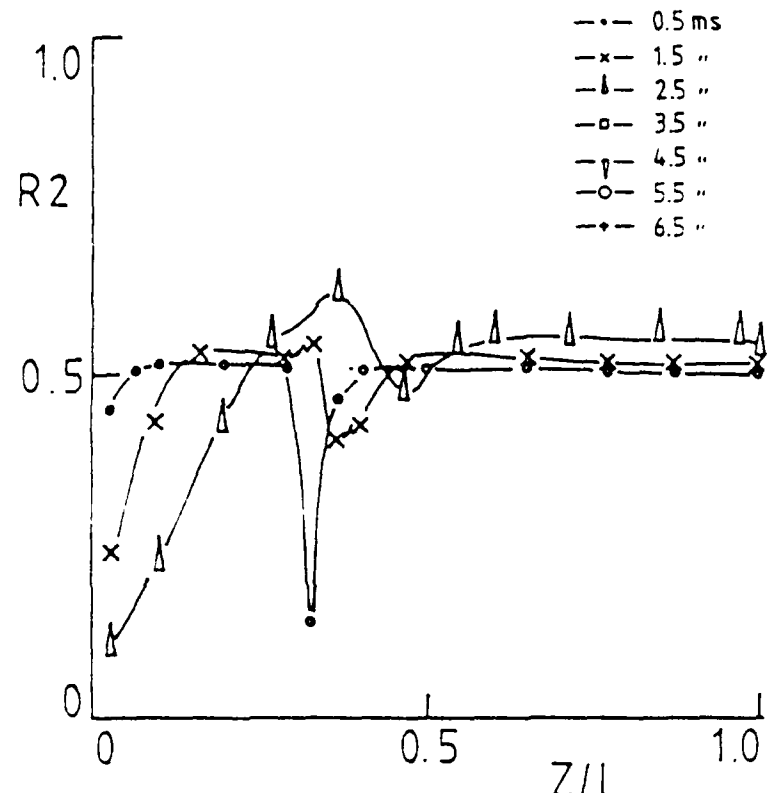
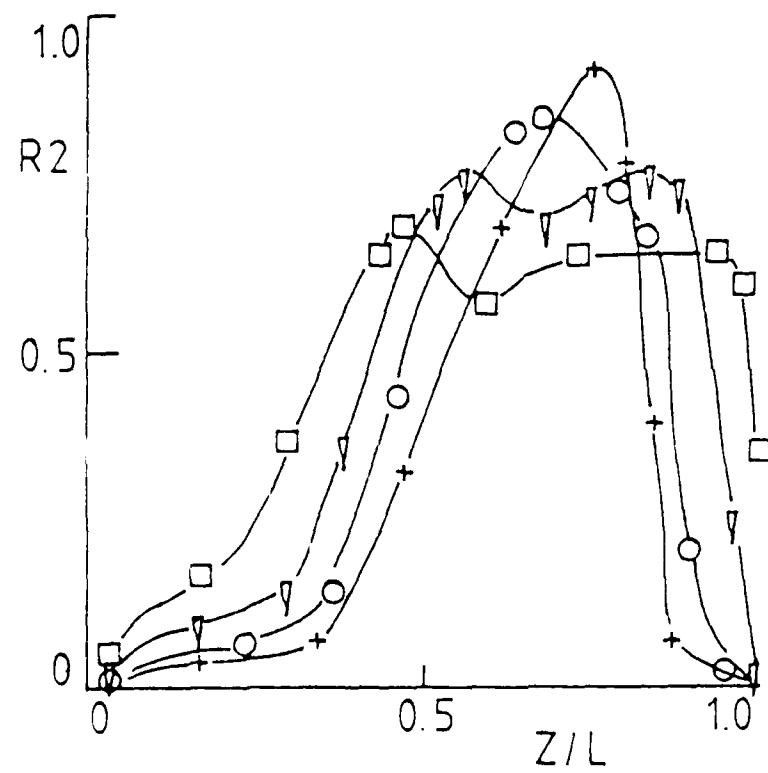


Figure 20



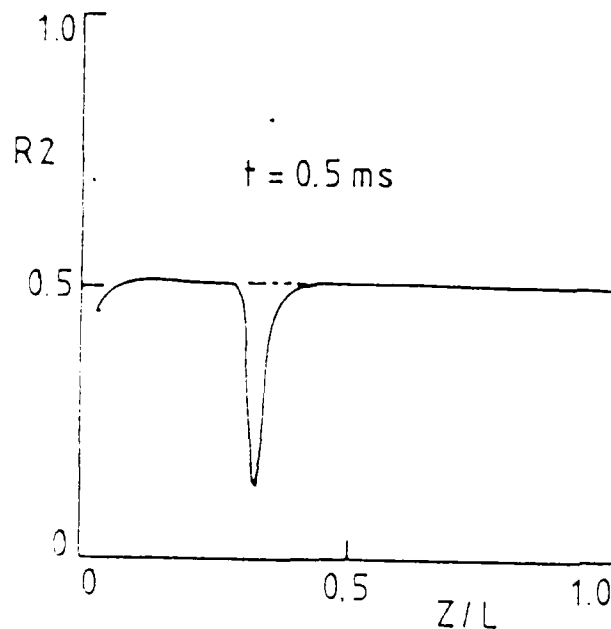
(a)



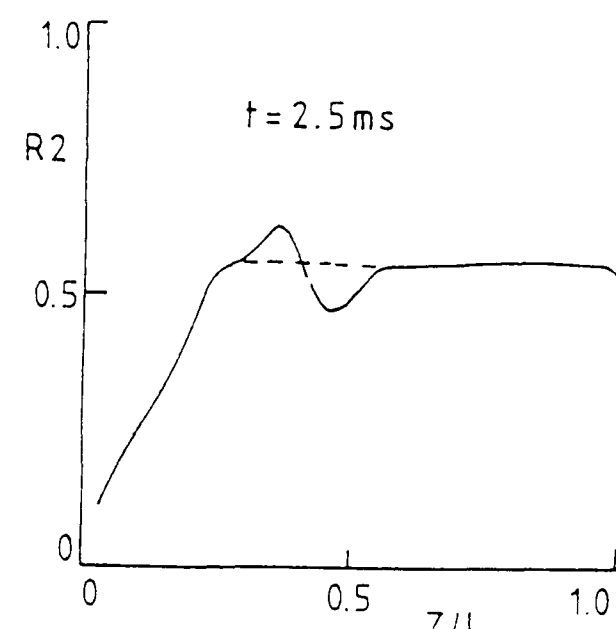
(b)

Figure 21

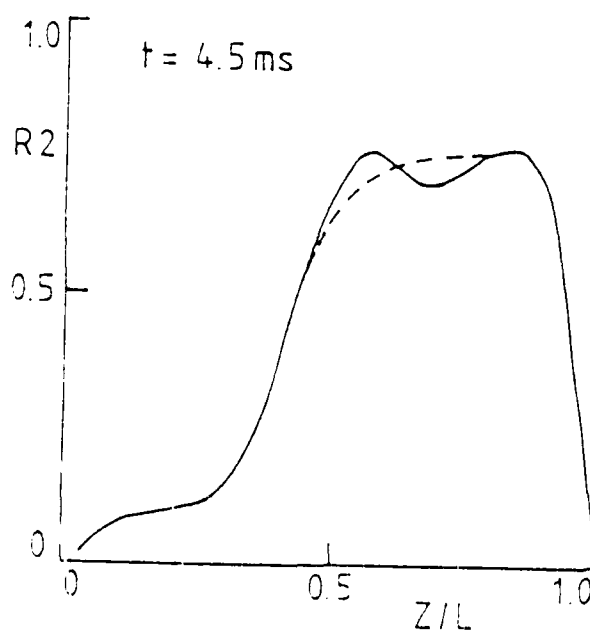
The particle volume fraction distribution history  
at  $r/R = 0.64$



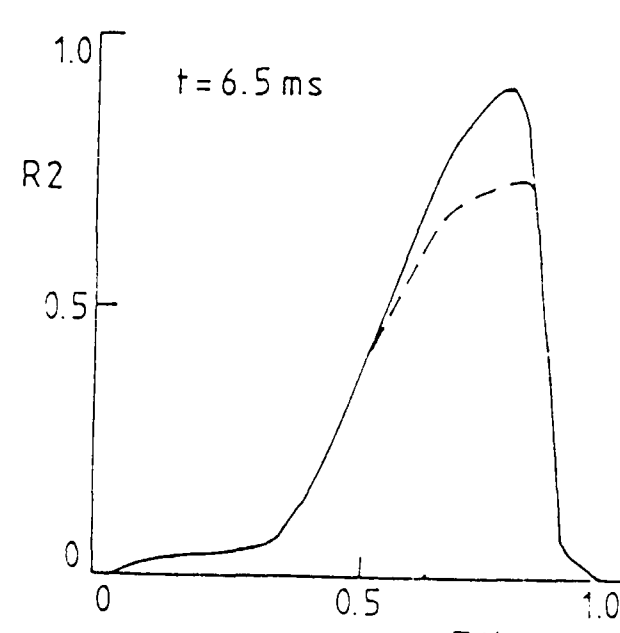
(a)



(b)



(c)



(d)

Figure 22

The particle volume fraction in the two calculations at  $r/R=0.64$

----- without initial non-uniformity  
 \_\_\_\_\_ with an initial non-uniformity

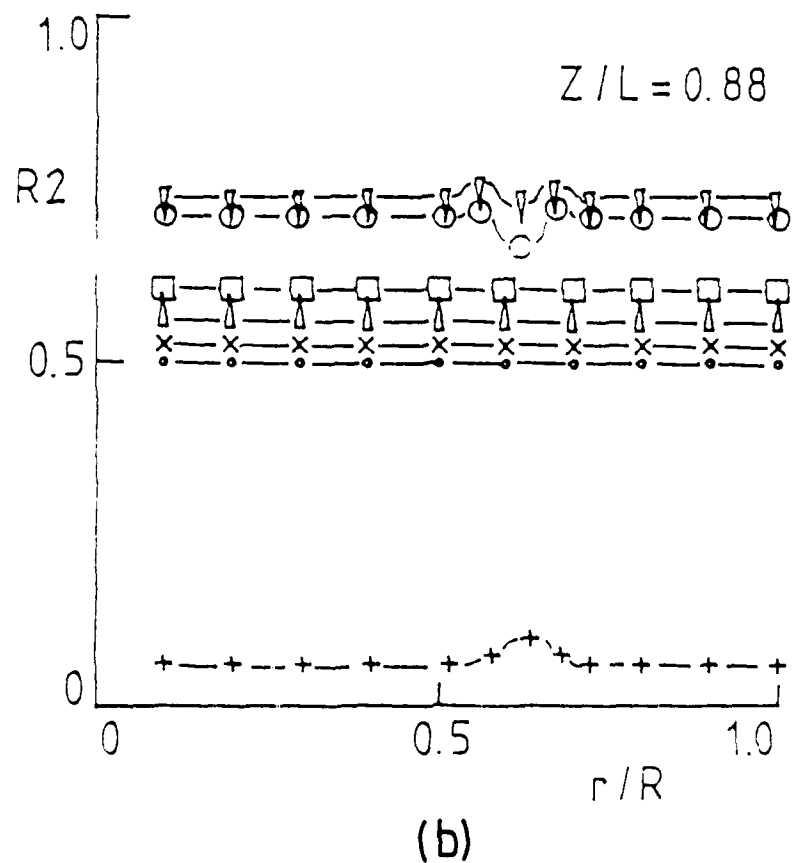
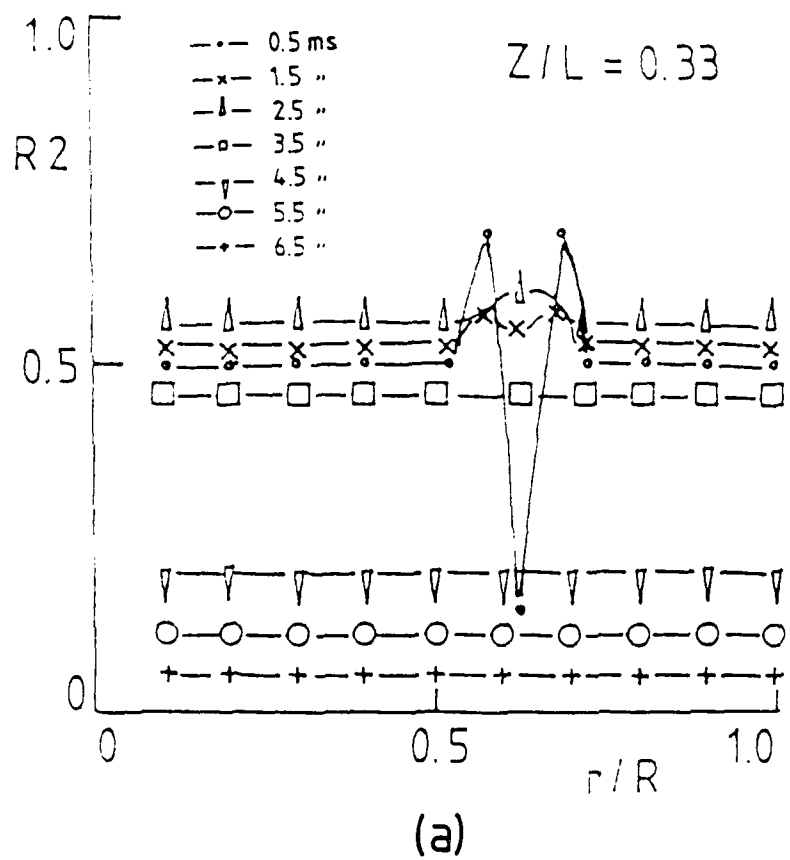


Figure 23

The particle volume fraction radial distribution history at (a)  $Z/L = 0.33$  and (b)  $Z/L = 0.88$

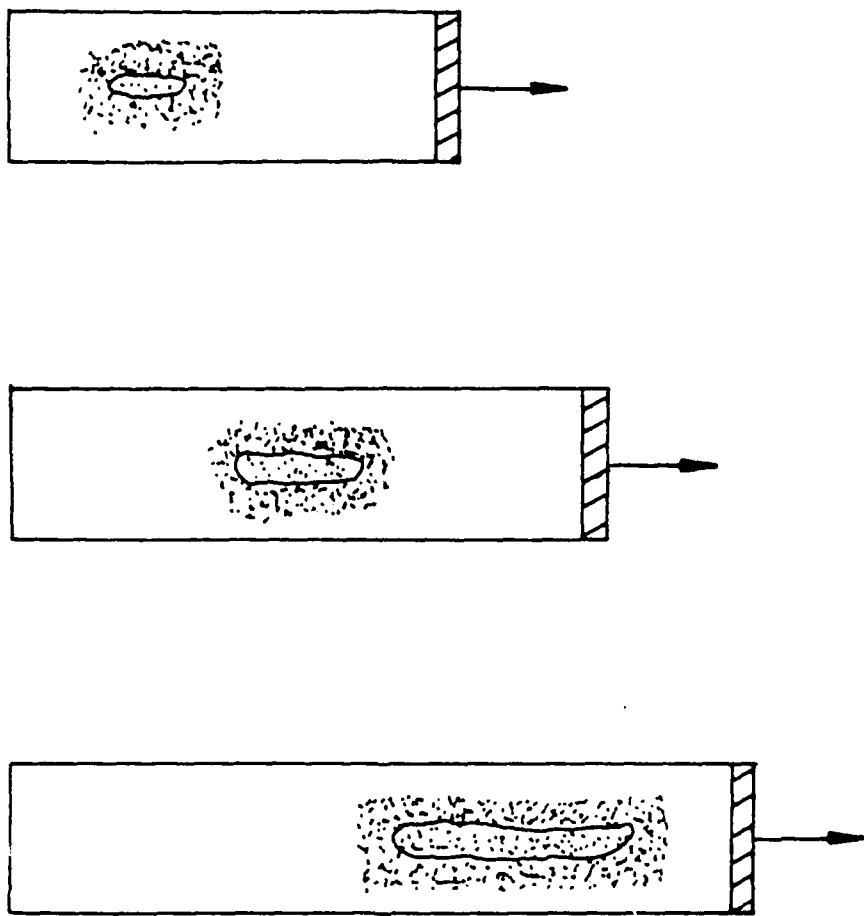


Figure 24

Sketch of the growth of an initial volume fraction non-uniformity in a gun barrel situation

E

W

D

87

DT / C